Journal of Sound and Vibration 595 (2025) 118787

Contents lists available at ScienceDirect

Journal of Sound and Vibration

journal homepage: www.elsevier.com/locate/jsvi

Numerical analysis of energy dissipation due to eddy currents in a vibrating beam

Mikel Brun *, Fernando Cortés, María Jesús Elejabarrieta

Department of Mechanics, Design and Industrial Management, University of Deusto, Avda. de las Universidades 24, 48007, Bilbao, Spain

ARTICLE INFO

Keywords:
Eddy currents damping
Vibrating beam
Motional induction
Numerical analysis
Finite difference method
Flexural-torsional modes

ABSTRACT

Vibration attenuation is a key aspect of mechanical engineering. One method to achieve this is through eddy currents, which can be generated in a vibrating system when a magnetic field is present, creating forces that oppose motion. This study examines a mechanical system consisting of a thin cantilever beam vibrating in a uniform and time-invariant magnetic field under steady-state conditions to understand the nature of energy dissipation and the relationship between motion, eddy currents, and damping forces. The calculation of eddy currents generally requires the use of complex numerical procedures. However, for systems with simple geometry, such as a cantilever beam, a recent numerical procedure based on the finite difference method, known for its simplicity in implementation, has been adapted and expanded to determine eddy currents under motional induction. A numerical application has been developed in which the vibration of a specific beam is characterised by its bending or torsional mode shapes, and the nature of the corresponding dissipative forces is analysed. Results indicate that the eddy currents are an effective means of dissipating energy at lower-order modes. Additionally, the direction of the applied magnetic field can induce coupling between bending and torsional vibrations.

1. Introduction

Electromagnetic forces can be generated when a conducting material interacts with a magnetic field via two induction mechanisms. On the one hand, transformer induction is stablished when a conductor is introduced into a time-varying magnetic field. On the other hand, motional induction occurs when a conductor moves within a time-invariant magnetic field. Additionally, both transformer and motional induction can occur simultaneously [1]. Induction generates currents known as Foucault currents within the conducting material and due to their swirling nature, they are also referred to as eddy currents.

These eddy currents can be either beneficial or detrimental, depending on the specific application. For instance, in Alternating Current (AC) machines, power loss due to Joule heating from eddy currents is undesirable [1,2]. Conversely, in damping applications, the damping forces produced by eddy currents are advantageous. Numerous fields are currently developing studies on eddy currents, such as braking applications [3,4], nonferrous metallic separation applications [5,6] or control applications for seismic activity using eddy current dampers such as the ones presented in [7,8], among others.

In mechanical vibration applications, eddy currents are of interest due to their energy dissipation capabilities, leading to numerous studies focusing on this topic. For example, in [9] an eddy current damper is designed to reduce vibrations in robotic milling, where the

* Corresponding author.
E-mail addresses: mikel.brun@opendeusto.es (M. Brun), fernando.cortes@deusto.es (F. Cortés), maria.elejabarrieta@deusto.es (M.J. Elejabarrieta).

https://doi.org/10.1016/j.jsv.2024.118787
Received 31 May 2024; Received in revised form 18 October 2024; Accepted 21 October 2024
Available online 22 October 2024

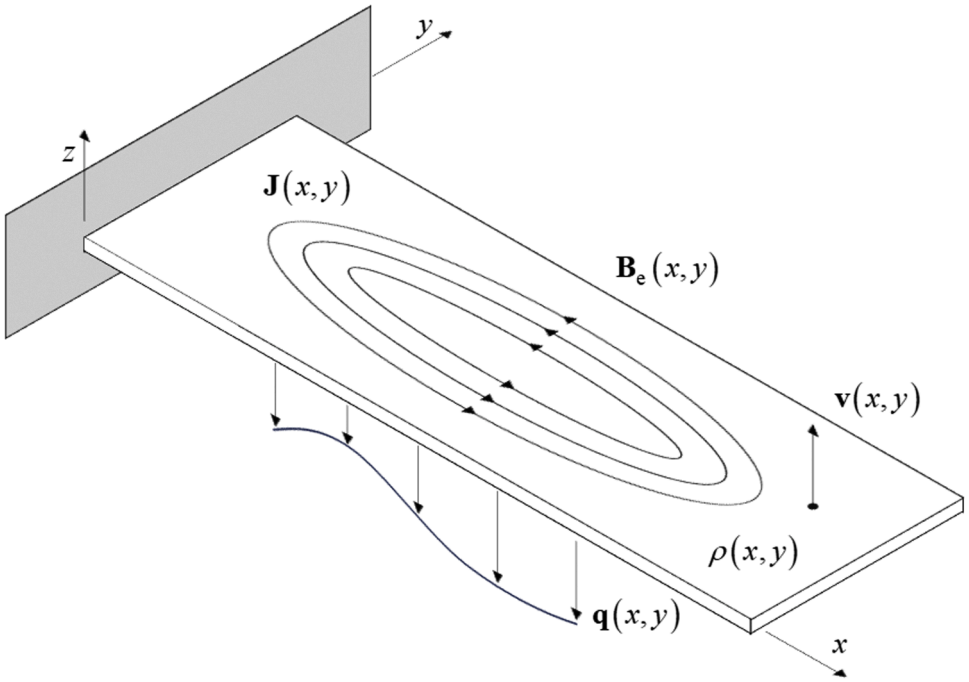

Fig. 1. Cantilever beam representation.

implementation of eddy currents can reduce vibrations by up to 22.1% and improve the robot's depth of cut by approximately 23.1%. Traditional viscoelastic passive damping techniques struggle to dissipate energy effectively at low frequencies. However, when combined with eddy currents, their effectiveness is enhanced across a broad frequency range [10]. In contrast, eddy current damping forces can be significant even at low frequencies. Beams are of particular interest in this context. For example, in [11], a ferromagnetic eddy current beam damper is proposed for a clamped-clamped beam configuration. In [12], a numerical model of a beam eddy current damper is developed for an aluminium beam to suppress vibrations, with no additional mass added to the beam as all the attenuation is achieved by an external static magnetic field. Another study in [10] compares experimental and numerical results on a vibrating sandwich beam structure, demonstrating that combining an eddy current damper with a viscoelastic sandwich is a highly effective method for attenuating vibrations up to 1 kHz, even at very low frequencies, due to the contribution of eddy current damping.

Applications involving eddy currents necessitate their modelling and resolution, often posing a challenging mathematical problem due to the nature of the governing equations where exact solutions rarely exist [1]. Thus, numerical procedures are required. Finite element formulations have been employed for many years. For example, in [13], a cantilever beam under a time-varying magnetic field is studied with six different formulations. In [14], finite elements are used to obtain magnetic field distributions in a 3-D environment. In [15], finite elements are used to solve a bounded domain containing conductors and dielectrics at low frequencies. In [16], a finite element formulation is developed to obtain magnetic field distributions by introducing the magnetic scalar potential in the non-conducting regions of the domain. More recently, in [17], a finite element formulation employing volume integral methods is proposed, defining novel face basis functions to construct the inductance matrix more efficiently. Improving computational times and numerical accuracy has been the focus of these numerical procedures over the years.

Among all existing numerical procedures, Nagel has developed two simple-to-implement numerical procedures based on the finite difference method to numerically obtain eddy currents when a rectangular sheet is subjected to a time-varying magnetic field. Specifically, in [18], eddy currents are directly obtained by defining staggered grids for the current components in the x and y directions. A preceding step involving the definition of the electric vector potential to determine the eddy currents is described in [19]. Both methods are simple to implement and can be easily adapted to various geometries, such as rectangular and circular plates or thin beams. However, a significant improvement in computation time is achieved in [19] compared to [18] as the number of variables in the problem is reduced, and because the matrix associated with the electric vector potential that is assembled is symmetric.

In short, many vibration applications found in the literature involving eddy currents focus on designing devices that can attenuate vibrations. Although the physical phenomenon of eddy currents is well known for this purpose, there are few studies focused directly on the dissipative nature of eddy currents generated in steady-state vibration for different modes of beams. An experimental modal analysis exists in [20], where the dynamic properties are analysed when an eddy current damper is used to attenuate vibrations on an aluminium cantilever beam. This paper aims to expand the knowledge presented in that analysis and study the energy dissipation capabilities of eddy currents generated on a vibrating thin paramagnetic conducting metallic beam in the presence of a time-invariant magnetic field for the lower-order mode shapes.

This article is structured as follows: after the introduction of Section 1, Section 2 details the system studied, including the

Table 1
Velocity field summary [21].

	Bending	Torsion
$v_r(x,y)$	$\frac{v_{\max}}{2}\left[\cosh\left(\frac{\lambda_r x}{L_x}\right) - \cos\left(\frac{\lambda_r x}{L_x}\right) - \kappa_r\left(\sinh\left(\frac{\lambda_r x}{L_x}\right) - \sin\left(\frac{\lambda_r x}{L_x}\right)\right)\right]$ where $\kappa_r = \frac{\sinh\lambda_r - \sin\lambda_r}{\cosh\lambda_r + \cos\lambda_r}$	$\frac{2v_{\max}}{L_y}\sin\left(\frac{\lambda_r x}{L_x}\right)(y - L_y/2)$
λ_r	$\cos\lambda_r\cosh\lambda_r + 1 = 0$	$\cos\lambda_r = 0$
ω_r	$\frac{\lambda_r^2 L_z}{{L_x}^2}\sqrt{\frac{E}{12\rho_v}}$	$\frac{\lambda_r L_y L_z}{L_x({L_y}^2 + {L_z}^2)}\sqrt{\frac{12cG}{\rho_v}}$
m_{eq}	$\frac{m}{4}$	$\frac{m}{6}\left(1 + \left(\frac{L_z}{L_y}\right)^2\right)$

Table 2
Geometric factor c as a function of the ratio L_y/L_z [21].

L_y/L_z	1	2	4	8	∞
c	0.281	0.286	0.299	0.312	1/3

description of the applied velocity fields to the beam. Section 3 describes the numerical method proposed by Nagel and further expands upon it to solve the eddy currents generated in the thin beam due to motional induction. Once the eddy currents are solved, the procedure to extract the parameters of interest to analyse the vibration attenuation is presented, which includes damping force distribution, damping torque distribution, Joule's losses, mechanical energy dissipated throughout the entire beam, power distribution and modal viscous damping ratio. Finally, in Section 4, an exhaustive numerical analysis is performed, aimed at studying the nature of the eddy currents, damping forces and dissipated power for the lower-order bending and torsional modes, considering different directions of the magnetic field.

2. Description of the problem

The system under study comprises a thin metallic paramagnetic cantilever beam, whose vibration is characterised by a stationary harmonic motion, with its velocity amplitude vector denoted as $\mathbf{v}(x,y)$. The beam is subjected to an external time-invariant or static magnetic field $\mathbf{B}_e(x,y)$ as illustrated in Fig. 1. The objective is to obtain and analyse the dissipative nature of the forces generated due to the eddy currents induced in the beam. In Fig. 1, the eddy currents are represented by the current density amplitude vector field $\mathbf{J}(x,y)$, and the damping forces by the surface force distribution amplitude vector $\mathbf{q}(x,y) = q(x,y)\hat{\mathbf{z}}$, both being harmonic due to the harmonic nature of the velocity.

The beam's dimensions in the x, y and z directions are its length L_x, width L_y and thickness, L_z, respectively, where $L_y < L_x$. The beam is considered thin, hence $L_z \ll L_x$, implying no variation of properties over its thickness, and therefore $\partial/\partial z = 0$ for any property. Its mechanical properties are characterised by its Young's modulus E and shear modulus G, and its electrical properties by resistivity $\rho(x,y)$ along the beam. The external magnetic flux density vector $\mathbf{B}_e(x,y)$ is given by

$$\mathbf{B}_e(x,y) = B_x(x,y)\hat{\mathbf{x}} + B_y(x,y)\hat{\mathbf{y}} + B_z(x,y)\hat{\mathbf{z}}, \tag{1}$$

where $B_x(x,y)$, $B_y(x,y)$ and $B_z(x,y)$ are its components in the x, y and z directions, respectively. The beam exhibits harmonic vibration, and its velocity field amplitude vector $\mathbf{v}(x,y)$ is determined by bending or torsional modes. Although the interaction between vibration and external magnetic field can modify the harmonic bending or torsional velocity fields, it has been demonstrated that for beams at resonance, the natural frequencies and mode shapes remain almost unchanged [20]. For small amplitude vibrations and according to the Euler-Bernoulli beam theory, this implies that there is only velocity in the z direction, i.e. $\mathbf{v}(x,y) = v(x,y)\hat{\mathbf{z}}$, where $v(x,y)$ represents the amplitude of the transverse velocity. The shape of the velocity field depends on whether a bending or torsional mode is being considered. Table 1 presents the velocity field amplitude $v(x,y)$ adopted by the beam for the $r-$th bending or torsional mode [21], where $v_{\max}$ is the desired maximum velocity amplitude, λ_r and ω_r are the eigenvalue and angular natural frequency corresponding to the $r-$th natural mode, respectively, ρ_v is the volumetric density of the beam, c is a geometric factor defined from the ratio L_y/L_z for $L_y > L_z$, as indicated in Table 2, m is the mass of the beam ($m = \rho_v L_x L_y L_z$), and m_{eq} is the modal mass of the beam equivalent to the mass of a single-degree-of-freedom system. It is noted that in the case of bending, the velocity field magnitude depends solely on x according to the mode shape, while in the case of torsion, it depends on both x and y.

The interaction between the motion of the beam and the external static magnetic field, i.e., motional induction, induces currents. In a steady state, since the velocity is harmonic at angular frequency ω_r, the currents are also harmonic at the same frequency, with the amplitude of the current density vector field expressed as $\mathbf{J}(x,y)$. Given the beam's small thickness, the currents manifest as eddies in the $x-y$ plane, with the amplitude of the eddy current densities given by the vector field

$$\mathbf{J}(x,y) = J_x(x,y)\widehat{\mathbf{x}} + J_y(x,y)\widehat{\mathbf{y}}, \tag{2}$$

where $J_x(x,y)$ and $J_y(x,y)$ are the amplitude of the components of the generated eddy current density in the x and y directions, respectively. For the hypothesis that the currents are uniform in the beam's thickness to hold, the skin depth condition [1] must be met for the $r-$th mode, given by

$$\delta_r = \sqrt{\frac{2\rho}{\mu_0 \omega_r}} > L_z, \tag{3}$$

where μ_0 is the permeability of free space. The skin depth condition of Eq. (3) is verified for all cases in the numerical analysis of Section 4. The eddy currents generate damping forces that oppose the velocity field in the z direction, which according to Lorentz force [1] is given by

$$\mathbf{F}(x,y) = \mathbf{J}(x,y) \times \mathbf{B}_e(x,y), \tag{4}$$

where $\mathbf{F}(x,y)$ represents the force per unit volume amplitude vector. The resultant force $\mathbf{F}(x,y)$ can be expressed as distributed pressure over the entire surface of the beam as

$$\mathbf{q}(x,y) = L_z \mathbf{F}(x,y) \tag{5}$$

where $\mathbf{q}(x,y)$ is the distributed pressure, and indicated in Fig. 1. The distributed pressure $\mathbf{q}(x,y)$ can be reduced on the axis of the beam to a distributed transverse force of density amplitude $w(x)$ given by

$$w(x) = \int_0^{L_y} q(x,y)\mathrm{d}y, \tag{6}$$

where $q(x,y)$ is the amplitude of the pressure, and a distributed torque of density amplitude $\gamma(x)$ given by

$$\gamma(x) = \int_0^{L_y} q(x,y)\left(y - L_y/2\right)\mathrm{d}y. \tag{7}$$

3. Numerical procedure for solving eddy currents with motional induction

To analyse the mechanical energy dissipation ability of the thin cantilever beam presented in Fig. 1, it is essential first to solve the eddy currents generated. For this purpose, the governing equations of the problem are introduced, the existing numerical procedure for solving the currents is presented and extended to include motional induction, and finally, the relevant parameters are extracted from these currents.

3.1. Electromagnetic equations for motional induction

The physical beam model under study is illustrated in Fig. 1. The governing equation of the beam is provided by the general form of Faraday's law, which in the quasi-static form [22] is given by

$$\nabla \times \mathbf{E} = -\dot{\mathbf{B}}_i - \dot{\mathbf{B}}_e + \nabla \times (\mathbf{v} \times \mathbf{B}_e), \tag{8}$$

where $\mathbf{E}$ is the electric field vector, $\mathbf{B}_i$ is the magnetic field density vector induced by eddy currents, $(\bullet)^{\cdot}$ denotes time derivative, $\dot{\mathbf{B}}_i = \mathbf{0}$ since self-inductance is neglected due to the focus on lower-order modes and the very thin thickness of the beam L_z [18]. Additionally, since the external magnetic field is assumed to be time-invariant, $\dot{\mathbf{B}}_e = \mathbf{0}$. Here, ∇ represents the nabla operator $\nabla = \frac{\partial}{\partial x}\widehat{\mathbf{x}} + \frac{\partial}{\partial y}\widehat{\mathbf{y}} + \frac{\partial}{\partial z}\widehat{\mathbf{z}}$, $\times$ denotes the cross product, and $\nabla\times$ is the curl operator. Although Eq. (8) is time-dependent, since the velocity field is harmonic according to the expressions in Table 1, the current density is also harmonic, and the term expressed for the velocity field in Eq. (8) represents its amplitude. Henceforth, all variables appearing as vectors in subsequent equations refer to their amplitudes. The local form of Ohm's law [1] is given by

$$\mathbf{E} = \rho \mathbf{J}, \tag{9}$$

which, when substituted into Eq. (8), results in

$$\nabla \times (\rho \mathbf{J}) = \nabla \times (\mathbf{v} \times \mathbf{B}_e). \tag{10}$$

Considering the principle of charge conservation, the continuity equation for steady-state currents is given by

$$\nabla \cdot \mathbf{J} = 0, \tag{11}$$

where $\nabla\cdot$ denotes the divergence operator, indicating that the current density field $\mathbf{J}$ is divergence-free or solenoidal. This implies that the $\mathbf{J}$ field [1] can be expressed as the curl of a vector potential $\mathbf{T}$, satisfying

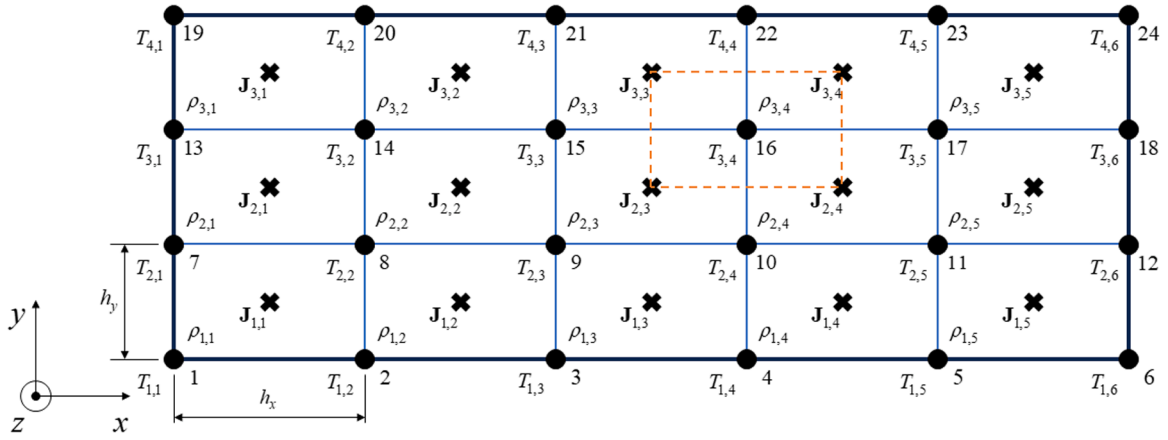

Fig. 2. Example of beam discretisation.

$$\mathbf{J} = \nabla \times \mathbf{T}, \tag{12}$$

which, for the thin beam considered, is defined as $\mathbf{T}(x,y) = T(x,y)\hat{\mathbf{z}}$, meaning that the currents satisfy

$$\mathbf{J}(x,y) = \frac{\partial T(x,y)}{\partial y}\hat{\mathbf{x}} - \frac{\partial T(x,y)}{\partial x}\hat{\mathbf{y}}. \tag{13}$$

Thus, Eq. (10) can be expressed as

$$\nabla \times (\rho \nabla \times \mathbf{T}) = \nabla \times (\mathbf{v} \times \mathbf{B}_e). \tag{14}$$

As the beam vibrates due to a velocity field in the $z-$direction only, the generated eddy currents do not exist in the $z-$ direction, consistent with the curl operator in Eq. (10) and the eddy current vector terms in Eq. (13). Expressing Eq. (14) in integral form, and applying Stokes' theorem to both sides results in

$$\oint_C (\rho \nabla \times \mathbf{T}) \cdot \mathbf{dl} = \oint_C (\mathbf{v} \times \mathbf{B}_e) \cdot \mathbf{dl}, \tag{15}$$

where C is an arbitrary contour within the limits of the beam, $\mathbf{dl}$ is an elementary vector distance along C and $\cdot$ represents the dot product. The solution of this equation provides the electric vector potential once boundary conditions are imposed. By inspecting Eq. (11), the normal component of the current at the edge of the beam must be zero, meaning $\mathbf{J} \cdot \hat{\mathbf{n}} = 0$, where $\hat{\mathbf{n}}$ is a unit normal vector. Thus, according to Eq. (13), the tangential derivative of T must be zero along the beam's edge. As a consequence, by choosing any arbitrary constant along the edge of the beam, Eq. (11) and Eq. (13) are compatible [19] and thus, for mathematical convenience, $T(x,y) = 0$ is preferred. Eq. (15) does not have an analytical solution and therefore, numerical procedures must be employed. The numerical method used to solve $\mathbf{T}$ from Eq. (15) is explained next.

3.2. Numerical method for motional induction

The numerical method employed by Nagel in [19] determines the electric vector potential $\mathbf{T}$ in a metallic, non-magnetic sheet subjected to a time-varying magnetic field. Extending this method to include motional induction involves evaluating the right-hand side of Eq. (15). To evaluate either side of the equation with this numerical method the metallic sheet is discretised into N rectangular cells with N_x cells in the $x-$ direction, each of length h_x and N_y cells in the $y-$ direction, each of length h_y. Each cell represents a block of constant current density $\mathbf{J}$, defined at its centre along with resistivity ρ, external magnetic flux density vector $\mathbf{B}_e$, and velocity field $\mathbf{v}$. By contrast, the electric vector potential $\mathbf{T}$ is defined at the nodes of the cells. For illustration, Fig. 2 depicts a discretisation example with 15 cells (5 in the $x-$direction and 3 in the $y-$ direction), where nodes are represented by dots $\bullet$ and cell centres by crosses $\times$.

Integration over the contour C in Eq. (15) corresponds to the dashed line contour in Fig. 2. The left-hand side of Eq. (15) is given by (detailed in [19,23])

$$\oint_C (\rho \nabla \times \mathbf{T}) \cdot \mathbf{dl} = a_0 T_0 + a_1 T_1 + a_2 T_2 + a_3 T_3 + a_4 T_4 \tag{16}$$

where

$$a_0 = \left(\frac{\rho_1 + \rho_2 + \rho_3 + \rho_4}{2}\right)\left(\frac{h_x}{h_y} + \frac{h_y}{h_x}\right), \tag{17}$$

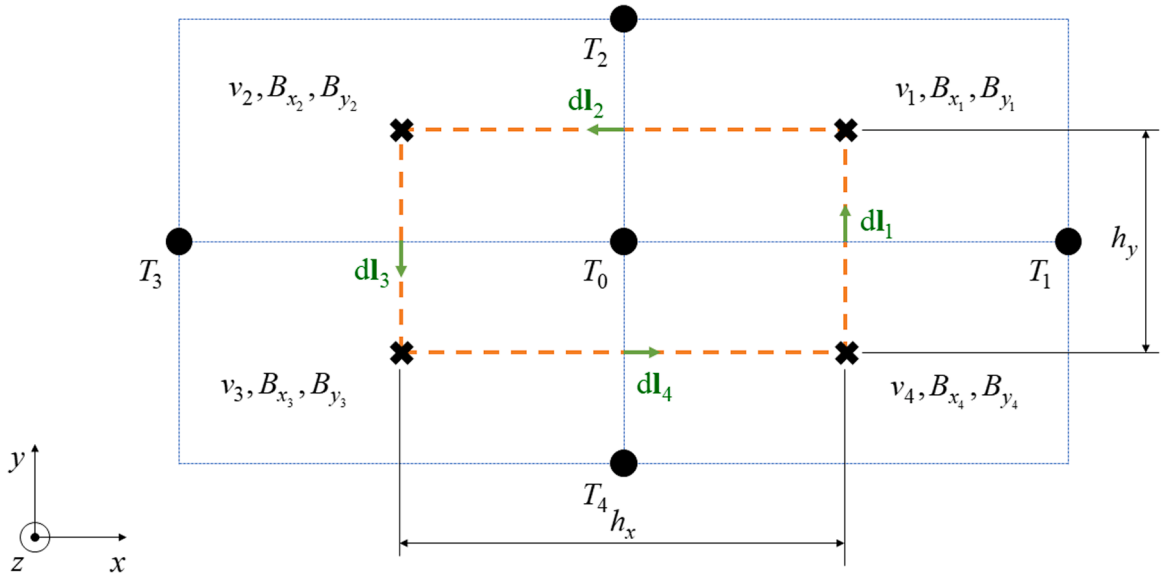

Fig. 3. Integration domain of a node.

$$a_1 = -\left(\frac{\rho_1 + \rho_4}{2}\right)\left(\frac{h_y}{h_x}\right), \tag{18}$$

$$a_2 = -\left(\frac{\rho_1 + \rho_2}{2}\right)\left(\frac{h_x}{h_y}\right) \tag{19}$$

$$a_3 = -\left(\frac{\rho_2 + \rho_3}{2}\right)\left(\frac{h_y}{h_x}\right) \tag{20}$$

and

$$a_4 = -\left(\frac{\rho_3 + \rho_4}{2}\right)\left(\frac{h_x}{h_y}\right), \tag{21}$$

in which, for notational convenience, the subscripts correspond to the nodes shown in Fig. 3.

Next, the right-hand side of Eq. (15), corresponding to motional induction, is evaluated, yielding

$$\oint_C (\mathbf{v} \times \mathbf{B}_e) \cdot \mathbf{dl} = \int_{l_1} (\mathbf{v} \times \mathbf{B}_e) \cdot \mathbf{dl}_1 + \int_{l_2} (\mathbf{v} \times \mathbf{B}_e) \cdot \mathbf{dl}_2 + \int_{l_3} (\mathbf{v} \times \mathbf{B}_e) \cdot \mathbf{dl}_3 + \int_{l_4} (\mathbf{v} \times \mathbf{B}_e) \cdot \mathbf{dl}_4, \tag{22}$$

where $\mathbf{dl}_i$ is the elementary vector distance on each edge of the dashed line contour in Fig. 3. The result of Eq. (22) yields

$$\begin{aligned} \oint_C (\mathbf{v} \times \mathbf{B}_e) \cdot \mathbf{dl} &= \frac{h_y}{2}\left(-v_3 B_{x_3} + v_4 B_{x_4} - v_2 B_{x_2} + v_1 B_{x_1}\right) \\ &+ \frac{h_x}{2}\left(-v_3 B_{y_3} - v_4 B_{y_4} + v_2 B_{y_2} + v_1 B_{y_1}\right), \end{aligned} \tag{23}$$

where v_i, B_{x_i} and B_{y_i} represent the velocity and the components of the external magnetic flux density vector $\mathbf{B}_e$ along the x and y directions at the respective corners of the contour. Subsequently, Eq. (16) and Eq. (23) are assembled. Although the system comprises $(N_x+1)(N_y+1)$ nodes, the previously mentioned boundary conditions are applied, i.e., $\mathbf{T} = \left\{ \mathbf{T}_{\text{edge}} \quad \mathbf{T}_{\text{uk}} \right\}^{\text{T}}$, where $\{\bullet\}^{\text{T}}$ is the transpose operator, and $\mathbf{T}_{\text{edge}} = \mathbf{0}$ on the nodes along the contour of the beam, resulting in a linear system of equations with $(N_x-1)(N_y-1)$ unknowns, which are solved from

$$\mathbf{M}\mathbf{T}_{\text{uk}} = \mathbf{b}, \tag{24}$$

where $\mathbf{M}$ is the matrix of coefficients resulting from the assembly of Eq. (16), $\mathbf{T}_{\text{uk}}$ is the vector of unknowns $\mathbf{T}$, and $\mathbf{b}$ is the vector of independent terms derived from the assembly of Eq. (23). It is noteworthy that, upon close inspection of each term in Eq. (16) at each node, the matrix $\mathbf{M}$ is symmetric.

To obtain the current density $\mathbf{J}$ associated with the electric vector potential $\mathbf{T}$ from Eq. (12), an additional step is required.

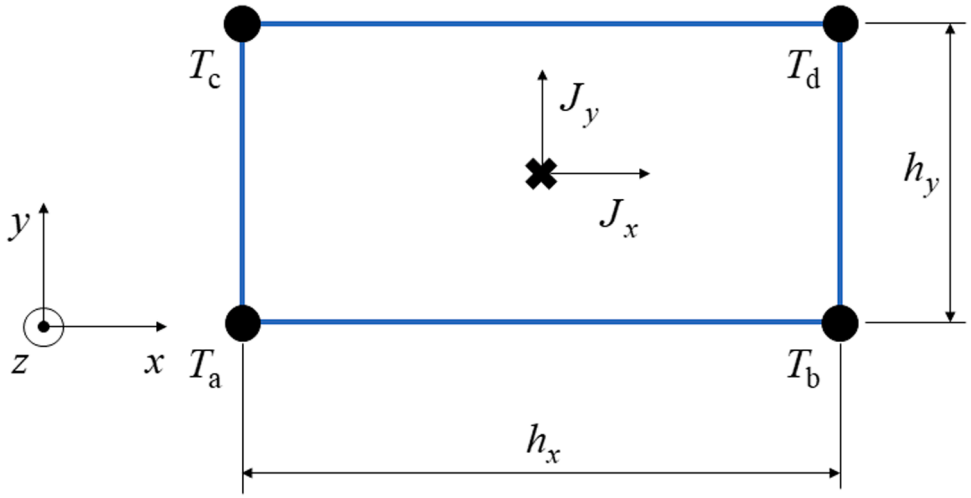

Fig. 4. Cell inspection to improved visualisation of eddy current calculation.

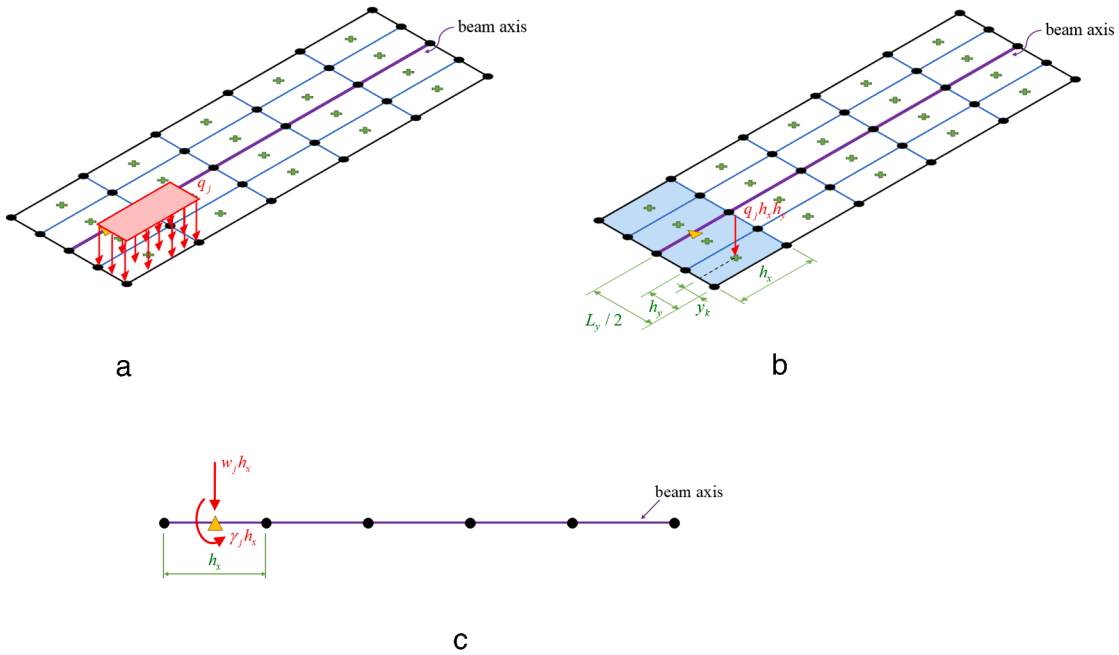

Fig. 5. Example diagram for evaluating force and torque distributions: (a) pressure over a cell; (b) equivalent force in a cell and (c) force and torque reduced to the beam's axis.

In Fig. 4, an arbitrary cell of the mesh is examined more closely, where T_i denotes the electric potential value at each corner, represented by dots, and the terms of the current density of the cell, defined at its centre, are J_x and J_y, represented by a cross. The current density for the cell is determined by averaging the finite differences around the corners, yielding

$$J_x = \frac{-T_a - T_b + T_c + T_d}{2h_y} \tag{25}$$

and

$$J_y = \frac{-T_a + T_b - T_c + T_d}{2h_x}. \tag{26}$$

Since these expressions provide the current values for a single cell, an assembly is conducted to account for all the cells in the beam, resulting in

$$\mathbf{J}_x = \mathbf{D}_x\mathbf{T} \tag{27}$$

and

$$\mathbf{J}_y = -\mathbf{D}_y\mathbf{T}, \tag{28}$$

where $\mathbf{J}_x$ and $\mathbf{J}_y$ are the vectors of the N current density components in the x and y directions, respectively, with each value corresponding to the current density at the centre of each cell, $\mathbf{D}_x$ is the matrix associated with Eq. (25), with each row corresponding to the equation of a cell, and $\mathbf{D}_y$ is the analogous matrix for Eq. (26), with the negative sign arising from the definition given in Eq. (13).

3.3. Energy dissipation parameters

After solving for the currents, damping force distribution, damping moment distribution, Joule's losses, mechanical power, power distribution, and modal viscous damping ratio are calculated.

3.3.1. Forces and moments distribution

The eddy currents generated due to motional induction induce dissipative forces and moments throughout the beam, which can now be computed. Fig. 5 illustrates the procedure for obtaining the transverse force distribution $w(x)$ and the bending moment distribution $\gamma(x)$ as explained below.

For a $j-$th given cell, based on the definition provided in Eq. (5), a distributed pressure is obtained over the surface of the cell, $\mathbf{q}\left(x_j, y_j\right) = q\left(x_j, y_j\right)\hat{\mathbf{z}}$ as represented in Fig. 5a by q_j, yielding

$$q\left(x_j, y_j\right) = L_z\left[J_x\left(x_j, y_j\right)B_y\left(x_j, y_j\right) - J_y\left(x_j, y_j\right)B_x\left(x_j, y_j\right)\right], \tag{29}$$

where x_j and y_j are coordinates at the centre of the $j-$th cell in the x and y directions, respectively. This pressure over the cell is uniform, as the calculated currents are also uniform within a cell. Thus, the resultant force at the centre of the $j-$th cell (indicated by the crosses in Fig. 5) is given by $q_j h_x h_y$, as represented in Fig. 5b. The aggregation of all the forces from the cells with the same x_j coordinate, like the filled ones shown in Fig. 5b, at the corresponding point along the beam's axis, indicated by a triangle, yields a resultant force and torque. These can be expressed in terms of densities w_j and γ_j, respectively, as shown in Fig. 5c.

The force distribution obtained for the $j-$th cell, based on the definition provided in Eq. (6), is given by

$$w(x) = h_y \sum_{k=1}^{N_y} q(x, y_k), \tag{30}$$

where y_k is the y coordinate of the $k-$th cell for those cells located at the same x. Since the currents are known only at the locations of the cell centres along the x direction (see Fig. 2), a linear interpolation is performed between the coordinates of consecutive cells in x to obtain a continuous damping force distribution.

Similarly, the damping torque distribution of density $\gamma(x)$, obtained for the $j-$th cell from Eq. (7), is given by (see Fig. 5c)

$$\gamma(x) = h_y \sum_{k=1}^{N_y} q(x, y_k)\left(y_k - L_y / 2\right). \tag{31}$$

3.3.2. Joule's losses and mechanical power

Motional induction generates currents that dissipate mechanical energy as heat within the material, in accordance with Joule's law. The differential form of Joule's heating [24] is expressed as

$$p_J(t) = \rho\mathbf{J}_{\text{ins}}(t) \cdot \mathbf{J}_{\text{ins}}(t) \tag{32}$$

where p_J is the instantaneous dissipated electrical power per unit volume, t denotes time, and $\mathbf{J}_{\text{ins}}$ represents the instantaneous current density vector field. The average power per cycle is obtained by averaging the above expression over an entire period t_0 resulting in

$$\overline{p}_J = \frac{1}{t_0}\int_0^{t_0} \mathrm{d}p_J(t)\mathrm{d}t, \tag{33}$$

where $\overline{p}_J$ is the average dissipated electrical power per unit volume. Due to the harmonic nature of the electric currents, Eq. (33) simplifies to

$$\overline{p}_J = \rho\frac{\mathbf{J} \cdot \mathbf{J}}{2}, \tag{34}$$

where $\mathbf{J}$ represents the amplitude of the current density vector field. The average power dissipated in the $j-$th cell is given by

Table 3
Beam geometry and material properties.

Parameter	Value
L_x(mm)	200
L_y(mm)	10
L_z(mm)	1
ρ_v(kgm^{-3})	2700
E (GPa)	65
G (GPa)	25
$\rho(\Omega\mu$m)	0.2

$$P_{J_j} = \rho h_x h_y L_z \frac{J_x^2\left(x_j, y_j\right) + J_y^2\left(x_j, y_j\right)}{2}. \tag{35}$$

Thus, the total average value of Joule's losses in the beam is

$$P_J = \sum_{j=1}^{N} P_{J_j}. \tag{36}$$

The energy dissipation in the beam can also be interpreted from another perspective, as it can be associated with the mechanical power derived from the Lorentz force in Eq. (4) as

$$\bar{p}_m = \frac{\mathbf{F} \cdot \mathbf{v}}{2}, \tag{37}$$

where $\bar{p}_m$ is the average mechanical power per unit volume,$\mathbf{v}$ represents the amplitude of the velocity field vector, and $\mathbf{F}$ the amplitude of the force per unit volume vector. In Eq. (37), only the force component in the z direction is relevant since velocity exists solely in that direction. Analogous to Eq. (34), the motion in this work is harmonic, and consequently, the force is harmonic as well. This harmonicity introduces a factor of 2 when averaging the instantaneous mechanical power. Expanding Eq. (37), the average power dissipated in the $j-$th cell becomes

$$P_{m_j} = h_x h_y \frac{q\left(x_j, y_j\right) v\left(x_j, y_j\right)}{2}. \tag{38}$$

Following the same procedure as for Joule's losses, the total average mechanical power in the beam is obtained as

$$P_m = \sum_{j=1}^{N} P_{m_j}. \tag{39}$$

It is also pertinent to study the power density along the beam. From the mechanical power calculated at each cell, the power density $p(x)$ is obtained as

$$p(x) = h_y \sum_{k=1}^{N_y} \frac{q(x, y_k) v(x, y_k)}{2}. \tag{40}$$

As with the distribution of the damping transverse force or the damping torque, a linear interpolation between the values at the cells is performed to obtain a continuous distribution.

Finally, as illustrated in Section 4, the numerical application demonstrates that the calculations of both Joule's losses and mechanical power yield the same global numerical result.

3.3.3. *Modal viscous damping ratio*

For low frequencies where self-inductance is negligible, as this study focuses on lower-order modes and the beam thickness L_z is very thin [18], the beam's vibration attenuated by eddy currents can be modelled by an equivalent classical mechanical model, such as the Kelvin-Voight model [25]. The modal viscous damping ratio for mode r, ζ_r, is obtained from the power losses P_m derived from the viscous force and is given by

$$\zeta_r = \frac{P_m}{m_{eq} \omega_r v_{max}^2}, \tag{41}$$

where m_{eq} is the modal mass of the beam, as provided in Table 1 for bending and torsion.

4. Numerical analysis

In this Section, dedicated to analysing the nature of the induced eddy currents, the results concerning currents and energy

Table 4
Cases of study for the aluminium cantilever beam.

	B_x(T)	B_y(T)	Modal velocity shape
Case 1	1	0	Bending
Case 2	0	1	Bending
Case 3	1	1	Bending
Case 4	1	0	Torsion
Case 5	0	1	Torsion
Case 6	1	1	Torsion

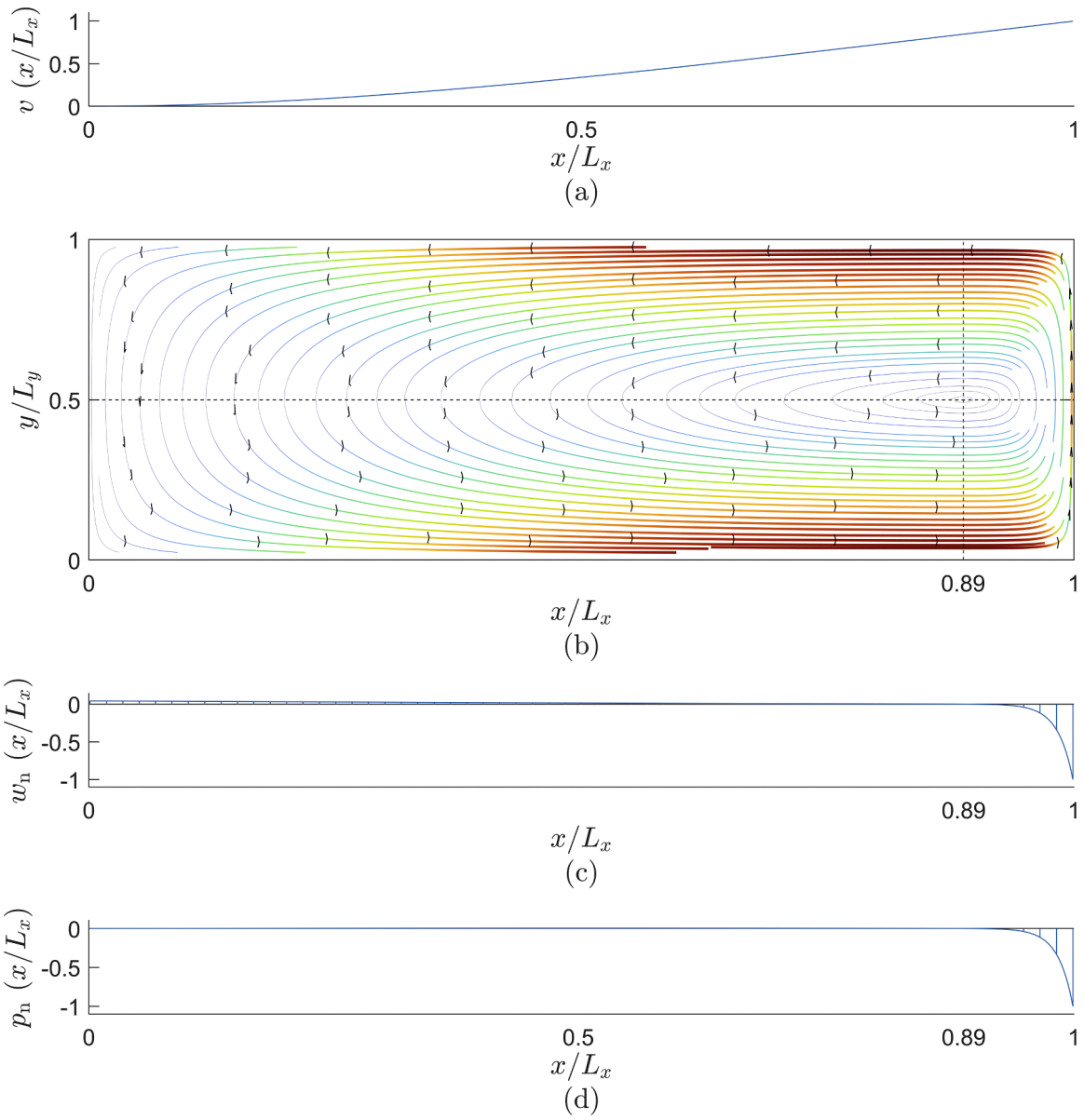

Fig. 6. Parameters for the first mode of Case 1: (a) modal velocity; (b) eddy currents density map; (c) normalised transverse force distribution and (d) normalised power distribution.

dissipation due to motional induction in a specific beam are solved for various bending and torsional modes. Specifically, the first four modes are examined in each case. The beam is analysed in a steady-state condition, with a uniform and time-invariant magnetic field applied in different directions.

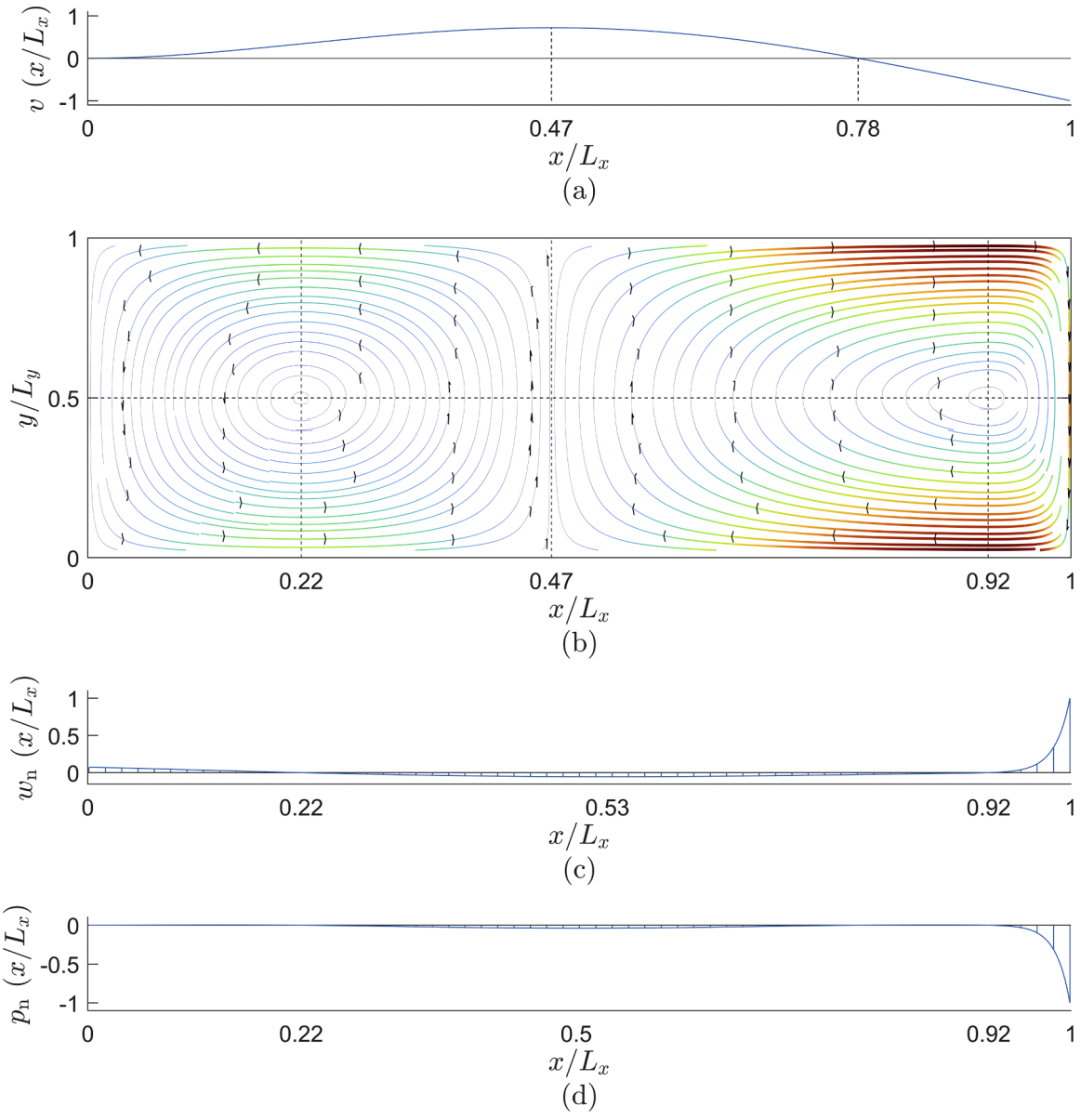

Fig. 7. Parameters for the second mode of Case 1: (a) modal velocity; (b) eddy currents density map; (c) normalised transverse force distribution and (d) normalised power distribution.

4.1. Beam numerical model

The geometry of the cantilever beam and its corresponding properties are outlined in Table 3. Aluminium has been selected as the conducting paramagnetic material for the beam due to its well-known high conductivity. The properties of the material are uniform throughout the entire beam.

The beam has been discretised into rectangular cells, with 421 cells along its length in the x direction and 21 cells along its width in the y direction, ensuring an equal density of elements per unit length in both directions. The beam's motion is defined by the modal shapes presented in Table 1, depending on whether bending or torsional motion is studied. All modes have been normalised; the maximum amplitude of the velocity field $v_{\max}$ in the velocity field expression given in Table 1 is set to 1ms^{-1}. The external magnetic field acting on the beam is time-invariant and uniform, with a unit magnitude applied in the x and/or y directions, as indicated in Table 4. For visual clarity, the distributions of force, moment, and power have been normalised with respect to their maximum values $w_{\max}$, $\gamma_{\max}$, and $p_{\max}$, respectively, and are thus denoted as $w_n = w/w_{\max}$, $\gamma_n = \gamma/\gamma_{\max}$, and $p_n = p/p_{\max}$.

The various cases under study are presented in Table 4, where the magnitude of the external magnetic field is specified.

The numerical results are subsequently presented and discussed for each case of study. For all cases, it has been confirmed that the

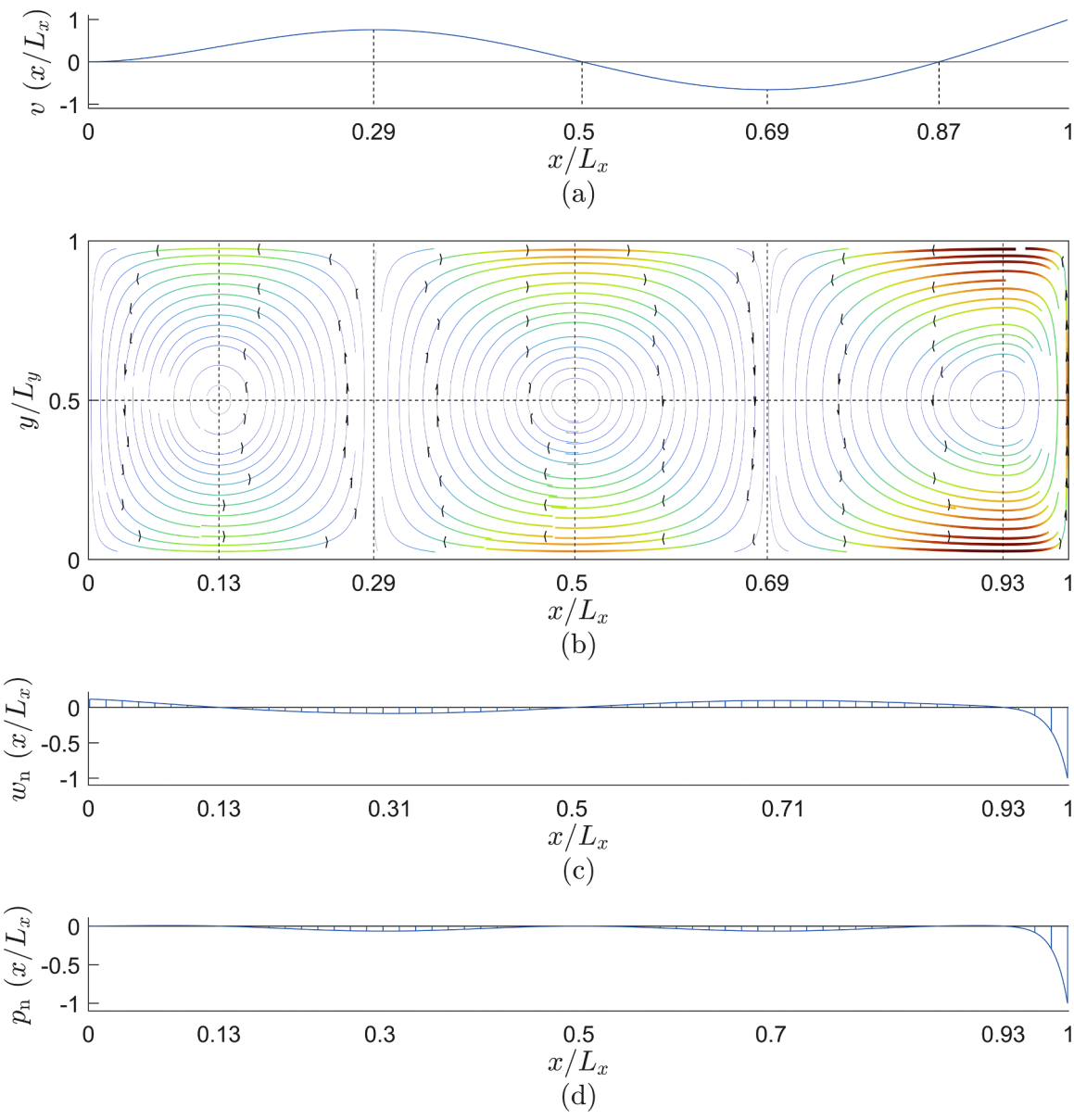

Fig. 8. Parameters for the third mode of Case 1: (a) modal velocity; (b) eddy currents density map; (c) normalised transverse force distribution and (d) normalised power distribution.

hypothesis of uniform current distribution across the beam's thickness, as stated in Eq. (3), is satisfied.

4.2. Beam results due to modal bending motion

The results for the first four modes are presented for Case 1, Case 2 and Case 3, corresponding to a bending modal shape.

4.2.1. Case 1

A unitary uniform and time-invariant magnetic field, applied solely in the $x-$ direction, is introduced as detailed in Table 4. The results obtained from the modal velocity of the first four bending modes, including the eddy currents density map, and normalised force and power distributions, are illustrated in Figs. 6-9. The maximum values of the normalised variables are provided in Table 5. Numerical results for the studied parameters for each mode are outlined in Table 6.

- With regard to eddy current maps ($\mathbf{J}$), it can be noted that the mode number corresponds to the number of eddies generated. When numbered from left to right, the currents rotate counter-clockwise in odd-numbered eddies and clockwise in even-numbered

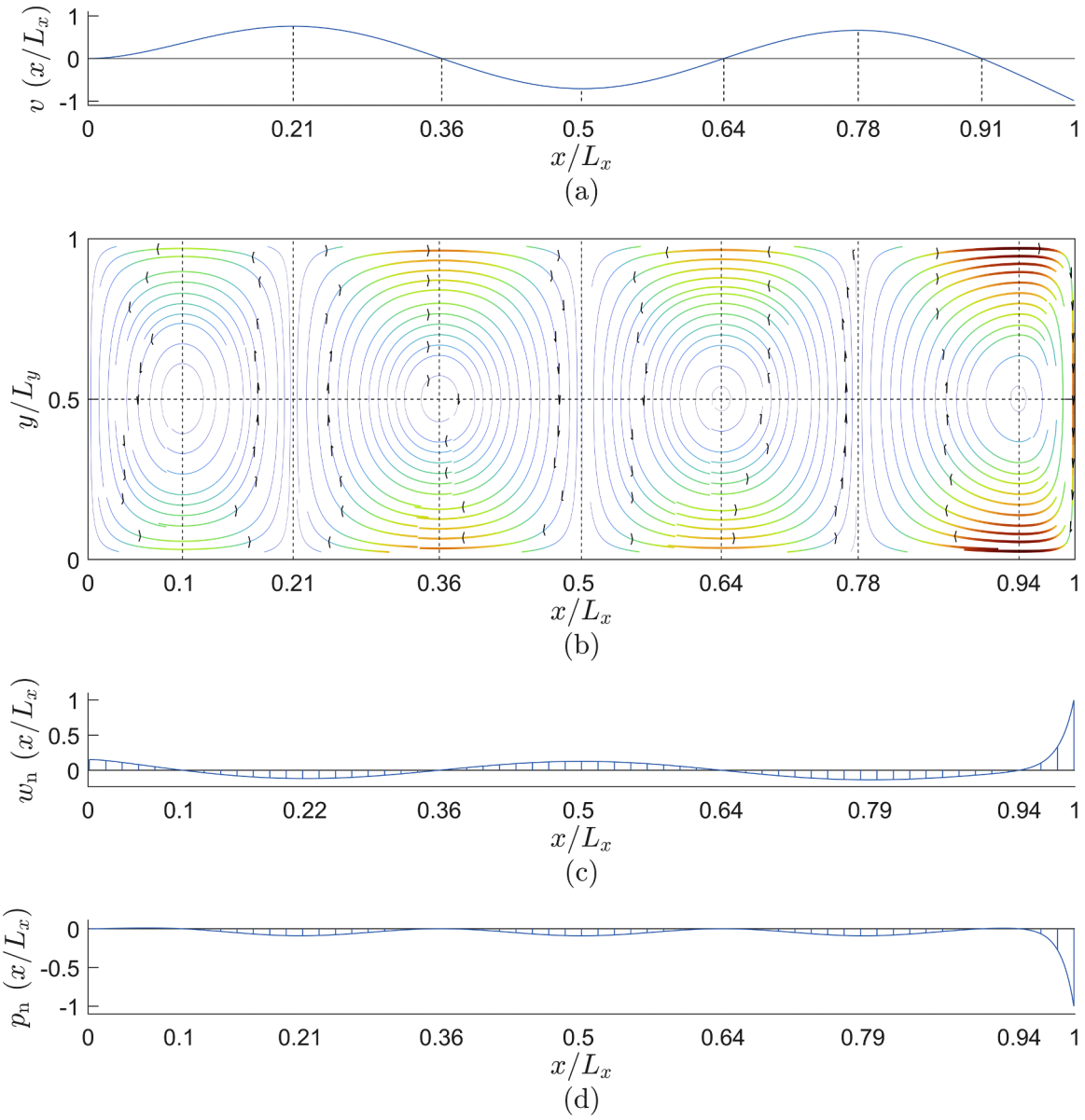

Fig. 9. Parameters for the fourth mode of Case 1: (a) modal velocity; (b) eddy currents density map; (c) normalised transverse force distribution and (d) normalised power distribution.

Table 5
Maximum values of force and power distributions for each mode of Case 1.

Mode	w_{max} (Nm^{-1})	p_{max} (Wm^{-1})
B1	0.854	0.427
B2	2.97	1.47
B3	4.86	2.41
B4	6.79	3.35

eddies. The highest current density is observed in the eddy closest to the free end of the cantilever beam, while those near the fixed end display lower values. The maximum current occurs near the top and bottom edges of the plate in the $y-$ direction, at the eddy nearest the free end. For modes 2 to 4, an eddy's border aligns with a point of maximum or minimum in the modal velocity. This can be explained by expanding Eq. (10), which leads to

Table 6
Resonance frequency, maximum value of the amplitude of the current density map in x and y directions, average power of Joule's losses, average mechanical power, and modal viscous damping ratio for each mode of Case 1.

Mode	ω_r (rads^{-1})	$J_{x_{\max}}$ (MAm^{-2})	$J_{y_{\max}}$ (MAm^{-2})	P_{J} (mW)	P_{m} (mW)	$\zeta_r(\times 10^{-3})$
B1	124.5	0.163	0.120	−1.18	−1.18	6.99
B2	780.2	0.561	0.415	−8.01	−8.01	7.61
B3	2185	0.898	0.680	−18.8	−18.8	6.38
B4	4281	1.22	0.950	−34.2	−34.2	5.92

$$\nabla \times (\rho \mathbf{J}) = \left(B_x \frac{\partial v(x,y)}{\partial x} + B_y \frac{\partial v(x,y)}{\partial y} \right) \widehat{\mathbf{z}}. \tag{42}$$

As seen in Eq. (42), since the applied magnetic field is uniform and the velocity field depends solely on x as shown in Table 1, the curl of the current density is 0 where the modal velocity is at a maximum or minimum. In Figs. 6-9, it can be observed that the centres of eddies for all modes in the $y-$direction are located at $y = L_y/2$. In the $x-$ direction, the locations of the eddy centres coincide with points where there is a change in curvature in the velocity field, except for the eddy centre closest to the free end. This exception arises because, in a cantilever beam subjected to modal bending vibration, the change in curvature occurs at the free end. However, since an eddy centre at the free end is not physically feasible due to the inability of currents to escape the beam, the eddy centre nearest the free end is positioned close to it. Consequently, this eddy is highly asymmetric compared to the others, leading to higher current densities near the free end. As the mode number increases, the location of the eddy centre closest to the free end in the $x-$direction shifts slightly towards the free end.

- The force distribution (w_{n}) is always positive at the fixed end, aligning with the direction of the modal velocity, and changes sign at each eddy centre in the $x-$ direction. Contrary to expectation, the force distribution and modal velocity do not align along the entire beam. The points at which the force distribution is 0 correspond to the eddy centres in the $x-$ direction, as $J_y \approx 0$ on this line, making the sum in Eq. (30) 0. The greatest contribution to damping occurs from the free end, where the maximum is reached in all cases, up to the eddy centre closest to the free end. For lower modes, the contribution of damping forces from the fixed end to the eddy centre nearest the free end in the $x-$direction is almost negligible, and as the frequency increases for higher-order modes, the damping force becomes more evenly distributed along the length of the beam. The maximum and minimum values of the damping forces between eddy centres tend to coincide with the points corresponding to a maximum or minimum of the modal velocity as the mode increases, or with the borders of the eddies. However, for lower-order modes such as mode 2, this is not the case. This discrepancy is due to the nature of the applied velocity field described in Table 1, where, for lower-order modes, the hyperbolic terms dominate, while as the mode number increases, the influence of the hyperbolic terms diminishes, and the velocity field approaches mathematically to a pure sinusoidal function. In mode 4, unlike in mode 2, the points of maximum or minimum modal velocity nearly coincide with those of the force distribution. Furthermore, as indicated by the numerical values of Table 5, the maximum value of the dissipative forces increases with the mode number.
- The power distribution (p_{n}) is always 0 at the fixed end and wherever the modal velocity is 0, since according to Eq. (40), no power is dissipated in the absence of velocity. It is also 0 at the eddy centres, as along a line coinciding with an eddy centre, $J_y \approx 0$ and thus the sum in Eq. (40) is 0. The power distribution is consistently positive near the fixed end, as the force distribution and modal velocity are aligned, but changes sign each time it passes through 0. Since the damping forces are concentrated from the free end to the centre of the eddy nearest to the free end, the power distribution exhibits a similar pattern. For higher-order modes, the power distribution tends to spread more evenly along the length of the beam. Analogous to the force distribution, the maximum and minimum values occurring between eddy centres in the power distribution tend to correspond, for higher modes, to the points where an eddy border exists or where the modal velocity reaches a maximum or minimum, as seen in mode 4. In contrast, for lower-order modes, such as mode 2, due to the hyperbolic nature of the modal velocity, the minimum value of the power distribution occurring between two eddy centres does not coincide with the eddy borders or with the maximum modal velocity. Additionally, as shown in Table 5, the maximum value of the power distribution increases with the mode number.
- Numerical results provided in Table 6 indicate that all parameters increase with frequency, except for the modal viscous damping ratio (ζ_r), which increases from mode 1 to mode 2, before decreasing. The fact that the modal viscous damping ratio tends to decrease at higher frequencies suggests that the energy dissipation capability of the eddy currents is greater for lower-order modes than for higher-order modes.
- The average power of Joule's losses (P_{J}) and the average mechanical power (P_{m}) are identical, indicating that whether energy dissipation is viewed from an electrical or mechanical perspective, the same information is obtained about the global energy dissipation in the cantilever beam. It is important to note, however, that although the global values of average power of Joule's losses and the average mechanical power are identical, their local values according to Eq. (34) and Eq. (37), do not necessarily match. In fact, in areas close to the fixed end, the average mechanical power is positive.

4.2.2. Case 2

A static and uniform magnetic field is applied exclusively in the $y-$ direction, as outlined in Table 4. In this case, no eddy currents are generated. This is due to the fact that the external magnetic field is uniform, and since the applied velocity field depends only on x, as indicated in Table 1, Eq. (42) consistently equals zero. This scenario underscores the critical importance of the direction of the

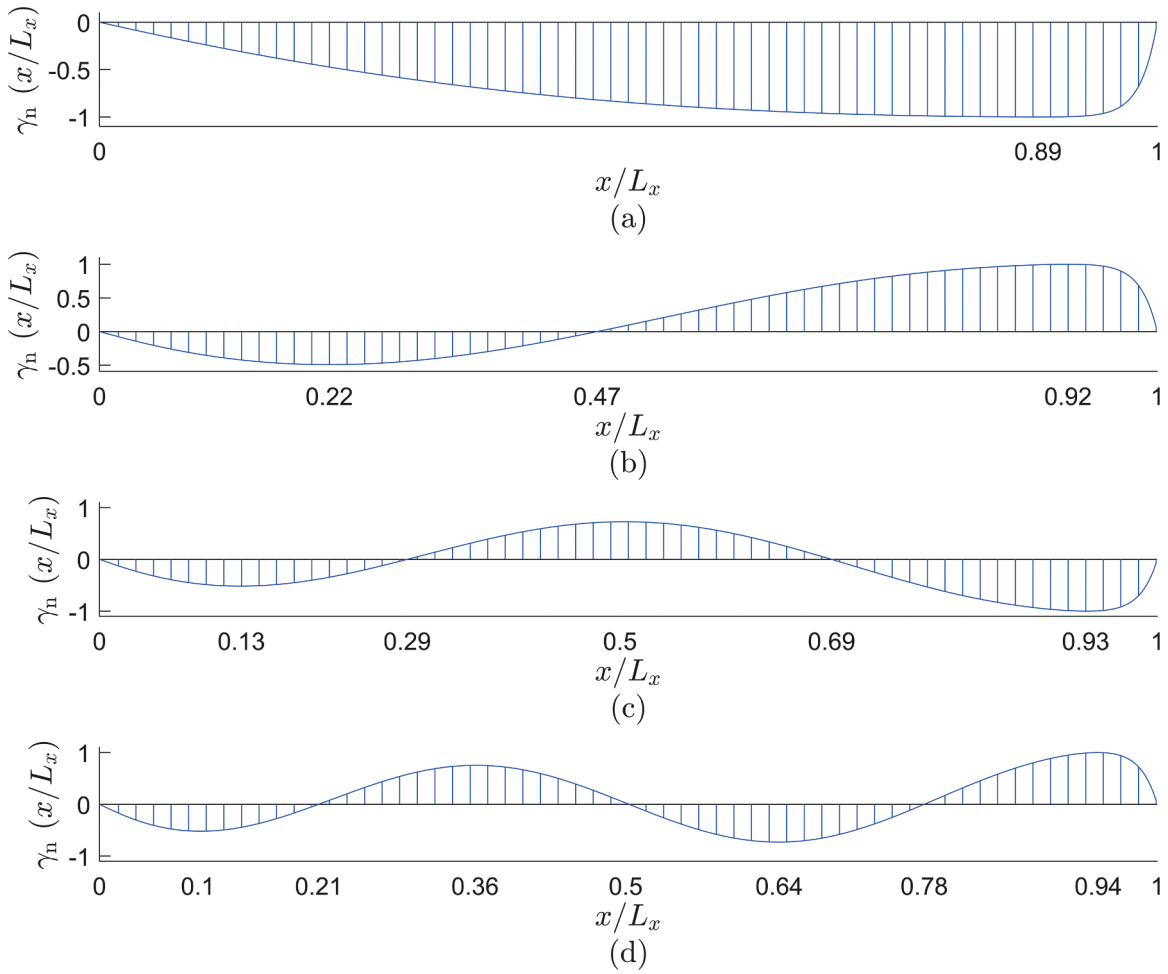

Fig. 10. Normalised torque distribution of Case 3: (a) mode 1; (b) mode 2; (c) mode 3 and (d) mode 4.

Table 7
Maximum values of torque distribution for each mode of Case 3.

Mode	γ_{max} (Nmmm^{-1})
B1	2.85
B2	9.78
B3	15.6
B4	21.2

external magnetic field in vibrating applications. Regardless of its magnitude, the orientation of the external magnetic field can result in no effect.

4.2.3. Case 3

The static and uniform external magnetic fields of Case 1 and Case 2 act simultaneously. In theory, since the B_y term in Eq. (42) does not influence the currents, because the velocity does not vary with y, the induced currents should remain the same as in Case 1. However, this term B_y alters the effect of the Lorentz force, as it interacts with J_x in Eq. (29) generating a torque according to Eq. (31). This torque is absent in Case 1, where the interaction between B_x and J_y does not produce such an effect due to the shape of the currents. The torque generated in this case results in coupling between bending and torsional motions. To emphasise the torque produced, its normalised distribution for the first four modes is shown in Fig. 10, with the corresponding maximum values listed in Table 7.

As this torque induces a torsional motion, the velocity generated by the torque must be added to the bending velocity. This implies that the problem can only be properly examined by coupling both movements simultaneously, which falls beyond the scope of this

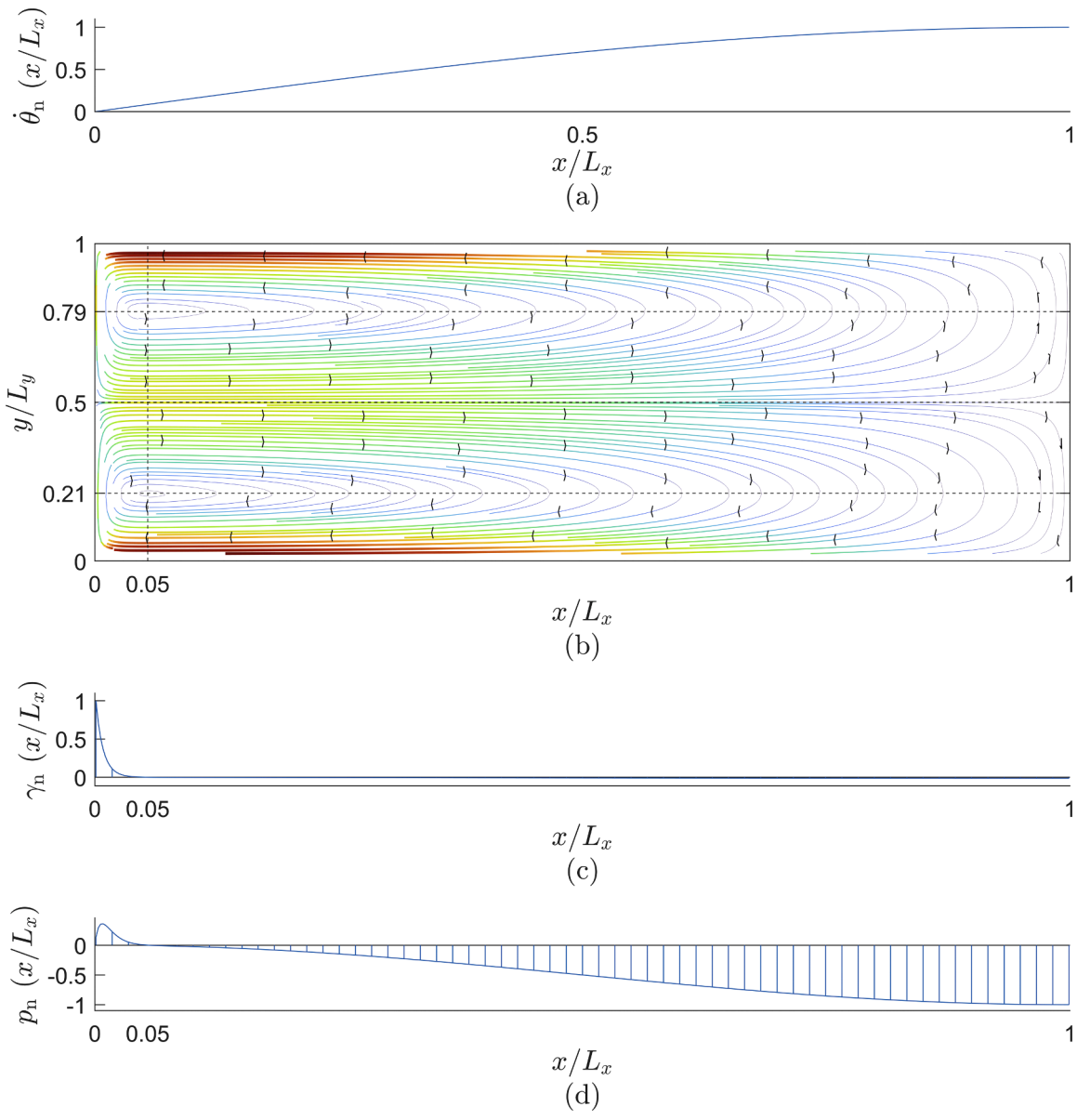

Fig. 11. Parameters for the first mode of Case 4: (a) modal twist velocity; (b) eddy currents density map; (c) normalised torque distribution and (d) normalised power distribution.

study. Although this coupling is not explored here, it is important to highlight its significance, as it arises solely from the interaction between the eddy currents and the external magnetic field.

4.3. Beam results due to modal torsional motion

The results for the first four torsional modes in Case 4, Case 5, and Case 6, associated with a modal torsional motion, are presented. In this instance, the modal twist velocity $\dot{\theta}$ is plotted rather than the transverse velocity field v as the former is characteristic of a cross-sectional motion. These two quantities are related by

$$v(x,y) = \dot{\theta}(x)\left(y - L_y/2\right). \tag{43}$$

For visualisation purposes, the modal twist velocity has been normalised with respect to its maximum value $\dot{\theta}_{\max}$ such that $\dot{\theta}_{\mathrm{n}} = \dot{\theta}/\dot{\theta}_{\max}$, where, for the beam under study and according to the values provided in Table 3, $\dot{\theta}_{\max} = 200\mathrm{rads}^{-1}$ for $v_{\max} = 1\mathrm{ms}^{-1}$.

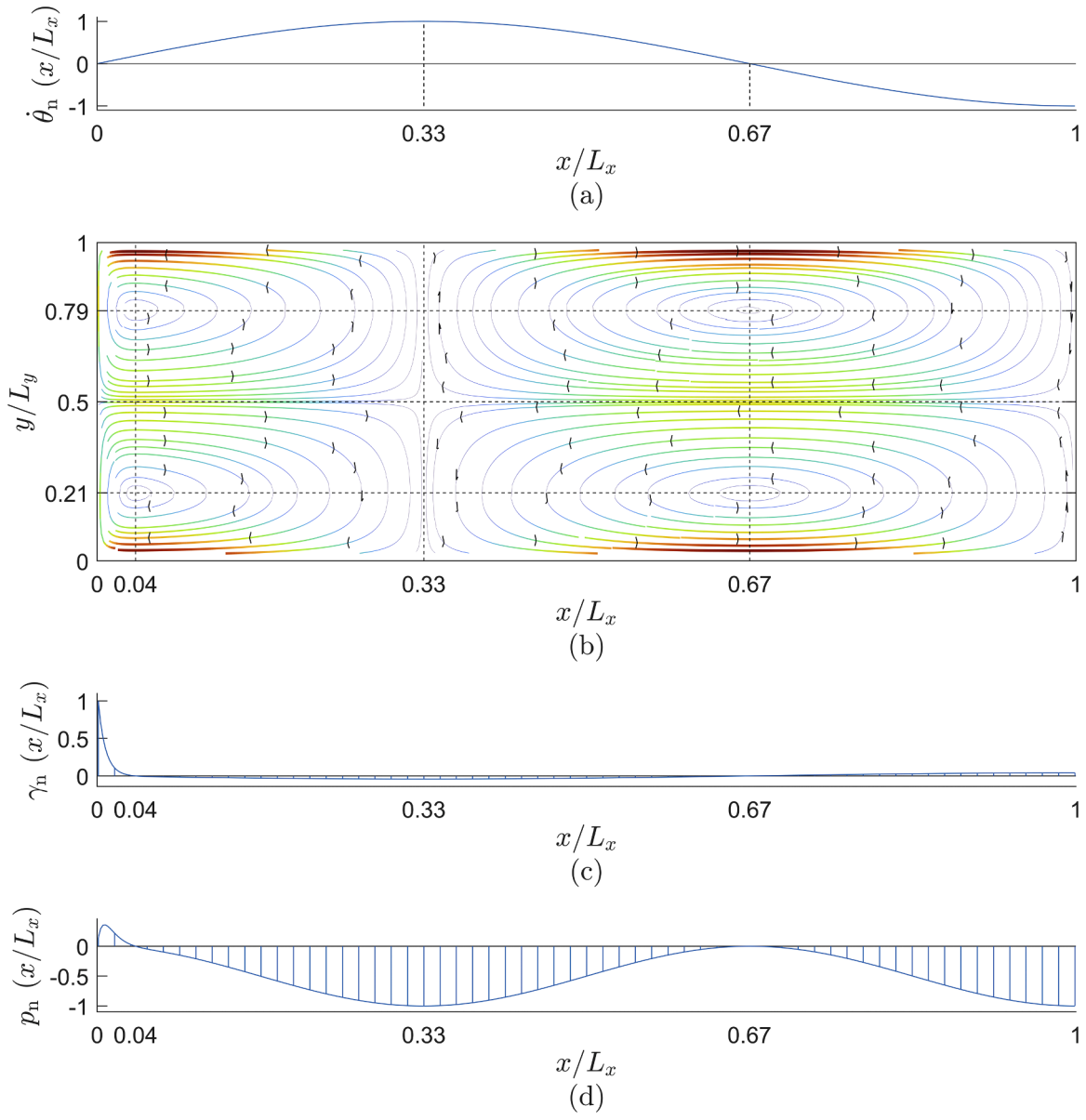

Fig. 12. Parameters for the second mode of Case 4: (a) modal twist velocity; (b) eddy currents density map; (c) normalised torque distribution and (d) normalised power distribution.

4.3.1. Case 4

A static, unitary, and uniform magnetic field is applied in the $x-$direction only, as specified in Table 4. The results derived from the normalised modal twist velocity for the first four torsional modes, including eddy currents density map, as well as the normalised torque and power distributions for these modes, are shown in Figs. 11-14. The maximum values of the normalised variables are listed in Table 8. Numerical results for the study parameters for each mode are outlined in Table 9.

- Two rows of eddies ($\mathbf{J}$) along the $x-$direction are generated for each case, each row containing a number of eddies corresponding to its mode. Each row of eddies is symmetric with respect to the beam axis, i.e., at $y = L_y/2$. The maximum values of the eddy currents are located near the top and the bottom of the beam. The eddy centres in the $y-$direction are always at fixed positions independent of the mode, and located at a distance of ± 0.29 from the beam axis. Similar to bending, in the $x-$ direction, the eddy centres are positioned at points where there is a change in curvature in the velocity profile, except for the eddy centre closest to the fixed end. In that case, the change in curvature would occur at the fixed end, and since it is not feasible for an eddy centre lo be located there, this first eddy centre is positioned near the fixed end. For modes 2 to 4, the points at which an eddy border occurs in the $x-$direction correspond to the locations where the modal twist velocity exhibits a maximum or minimum, as this is the only way to satisfy Eq.

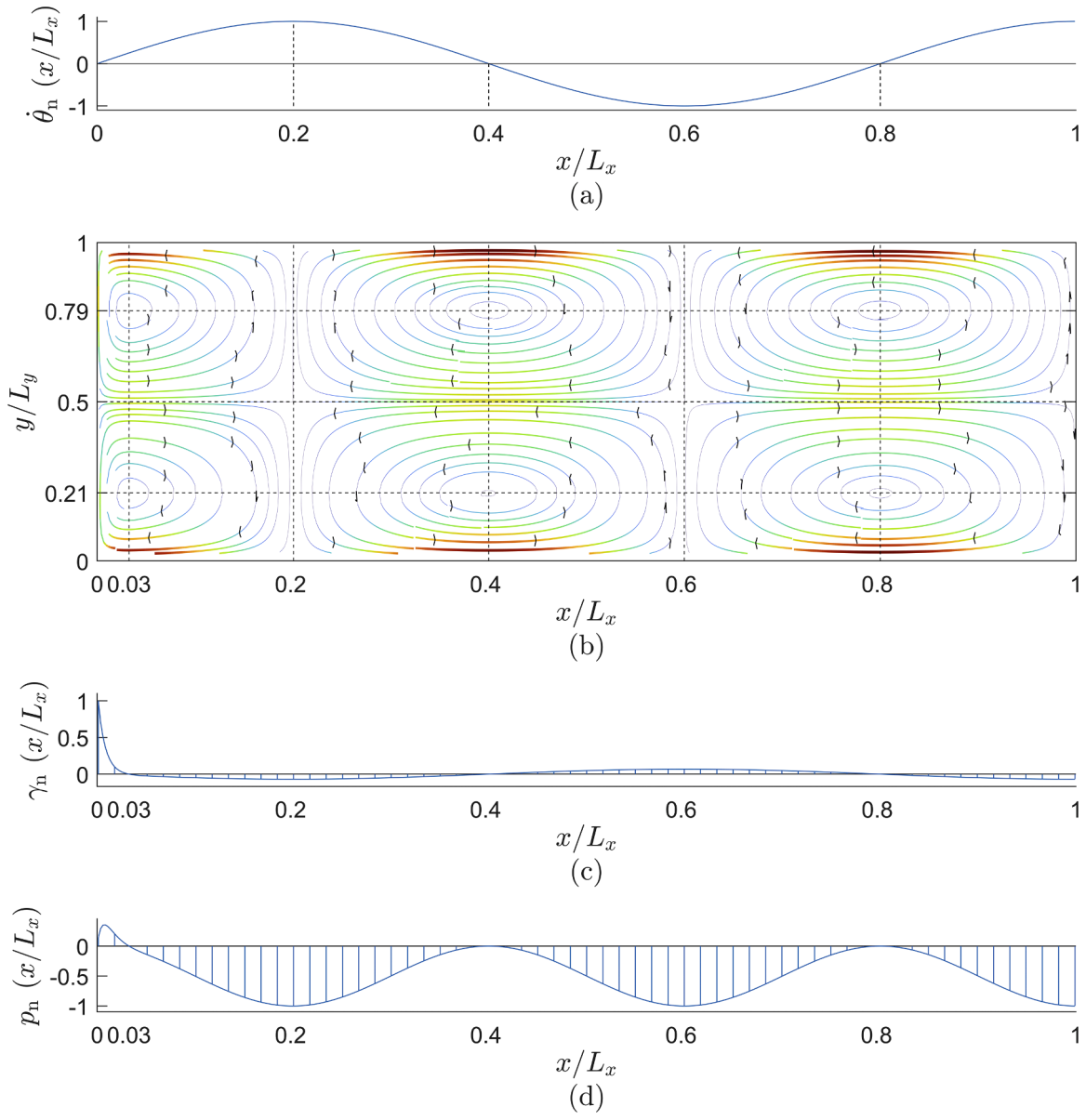

Fig. 13. Parameters for the third mode of Case 4: (a) modal twist velocity; (b) eddy currents density map; (c) normalised torque distribution and (d) normalised power distribution.

(42) with the velocity field given in Eq. (43), where the current density curl is 0. Analogous to bending, the eddy centres nearest the fixed and free ends move closer to the ends as the mode number increases.

- The torque distribution (γ_n) is positive at the fixed end, and changes sign at each eddy centre in the $x-$ direction. From the fixed end to the nearest eddy centre in the $x-$ direction, the torque distribution and modal twist velocity are aligned, but beyond that point, towards the free end, they oppose one another, as expected. The points at which the torque distribution reaches a maximum or minimum between eddy centres in the $x-$direction coincide with the eddy borders or locations where the modal velocity is at its maximum or minimum because the current density curl is 0 at those points. The torque distribution is concentrated near the fixed end, but as the mode number increases, it becomes more evenly distributed along the beam's length. According to the maximum torque values presented in Table 8, the torque increases as the mode number rises.
- The power distribution (p_n) starts at zero at the fixed end, where there is no velocity, and it is positive from the fixed end to the nearest eddy centre in the $x-$ direction. It becomes negative over the remaining length of the beam, reaching zero at each eddy centre in the $x-$direction or where the modal velocity is 0. The points where the minimum power distribution values between eddy centres occur correspond to the locations where the modal velocity reaches a maximum or minimum, or where an eddy border

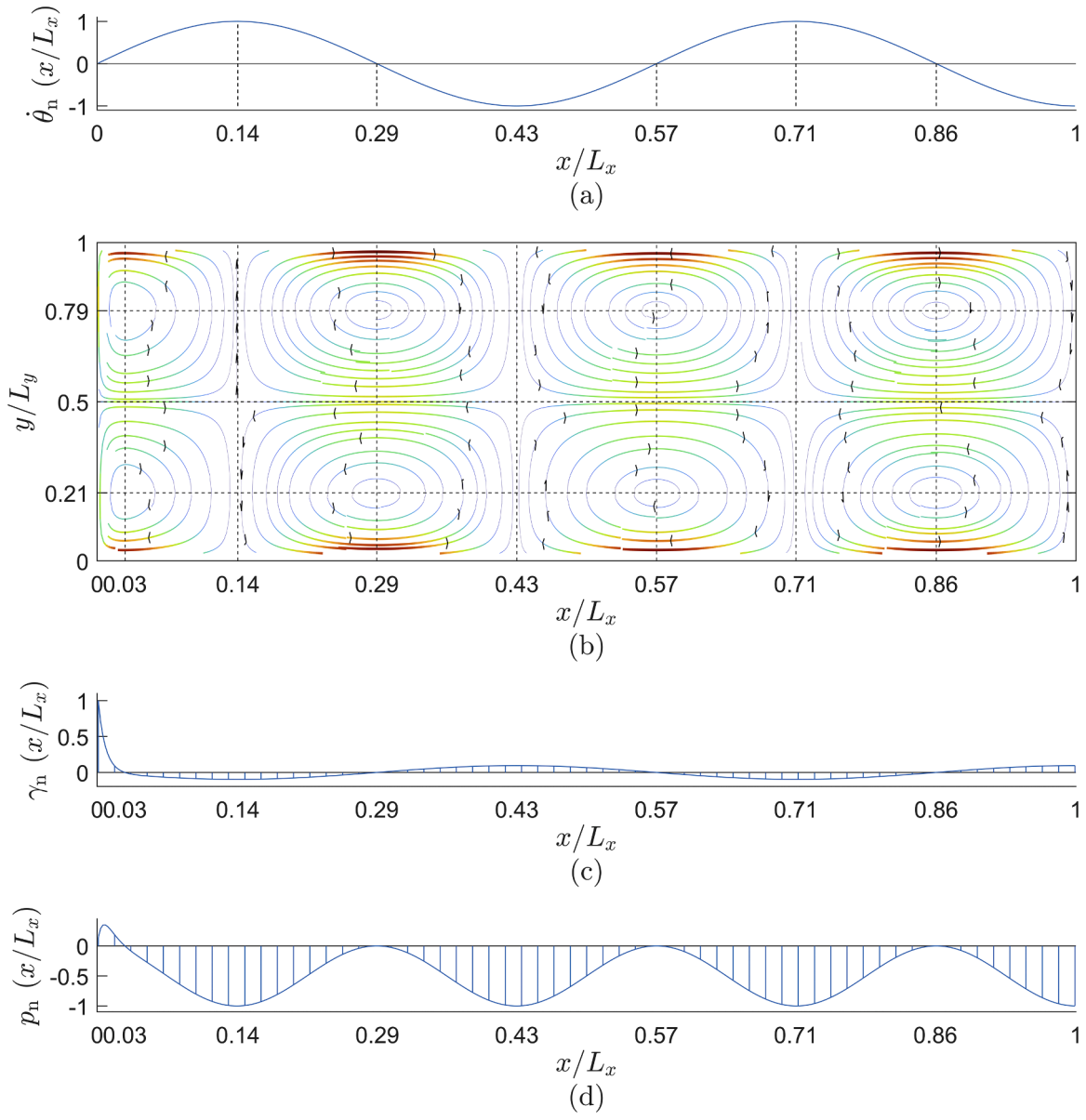

Fig. 14. Parameters for the fourth mode of Case 4: (a) modal twist velocity; (b) eddy currents density map; (c) normalised torque distribution and (d) normalised power distribution.

Table 8
Maximum values of torque and power distributions for each mode of Case 4.

Mode	γ_{max} (Nmmm^{-1})	p_{max} (mWm^{-1})
T1	0.618	0.847
T2	1.85	7.61
T3	3.08	21.1
T4	4.29	41.2

exists in the $x-$ direction. Numerical results from Table 8 show that the maximum power distribution increases as the mode number rises.

- All parameters in Table 9 increase as the frequency rises, indicating that for torsional motion, when an external magnetic field is applied along the length of the beam, the energy dissipation capability of the induced eddy currents improves at higher frequencies compared to lower ones, as reflected by the increase in the modal viscous damping ratio.

Table 9
Resonance frequency, maximum value of the amplitude of the current density map in x and y directions, average power of Joule's losses, average mechanical power, and modal viscous damping ratio for each mode of Case 4.

Mode	ω_r (rads^{-1})	$J_{x_{\max}}$ (MAm^{-2})	$J_{y_{\max}}$ (MAm^{-2})	P_J (mW)	P_m (mW)	ζ_r ($\times 10^{-5}$)
T1	4578.8	0.0561	0.0341	−0.0833	−0.0833	2.00
T2	13736	0.169	0.102	−0.749	−0.749	6.00
T3	22894	0.281	0.170	−2.08	−2.08	9.98
T4	32052	0.392	0.236	−4.05	−4.05	13.9

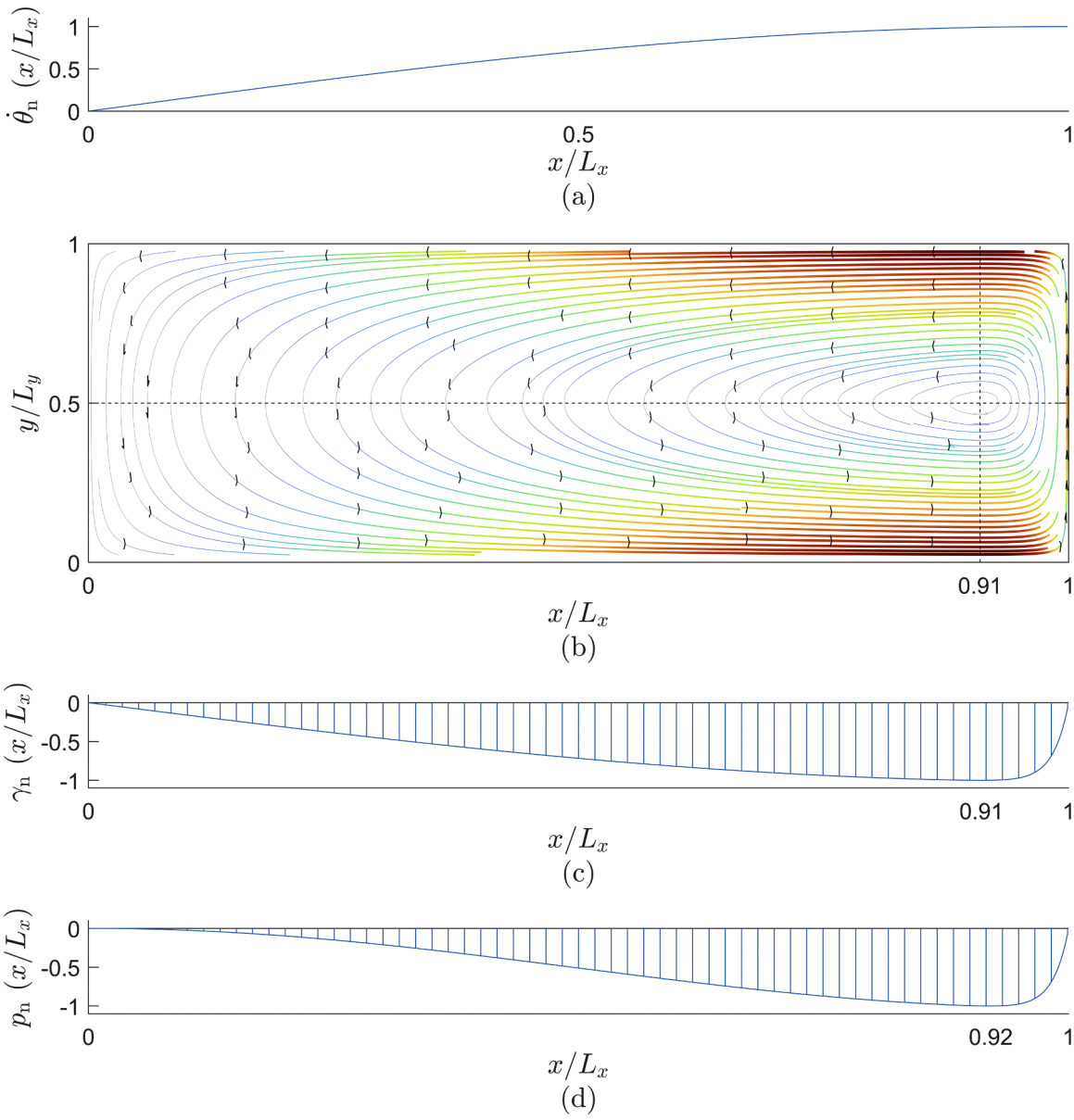

Fig. 15. Parameters for the first mode of Case 5: (a) modal twist velocity; (b) eddy currents density map; (c) normalised torque distribution and (d) normalised power distribution.

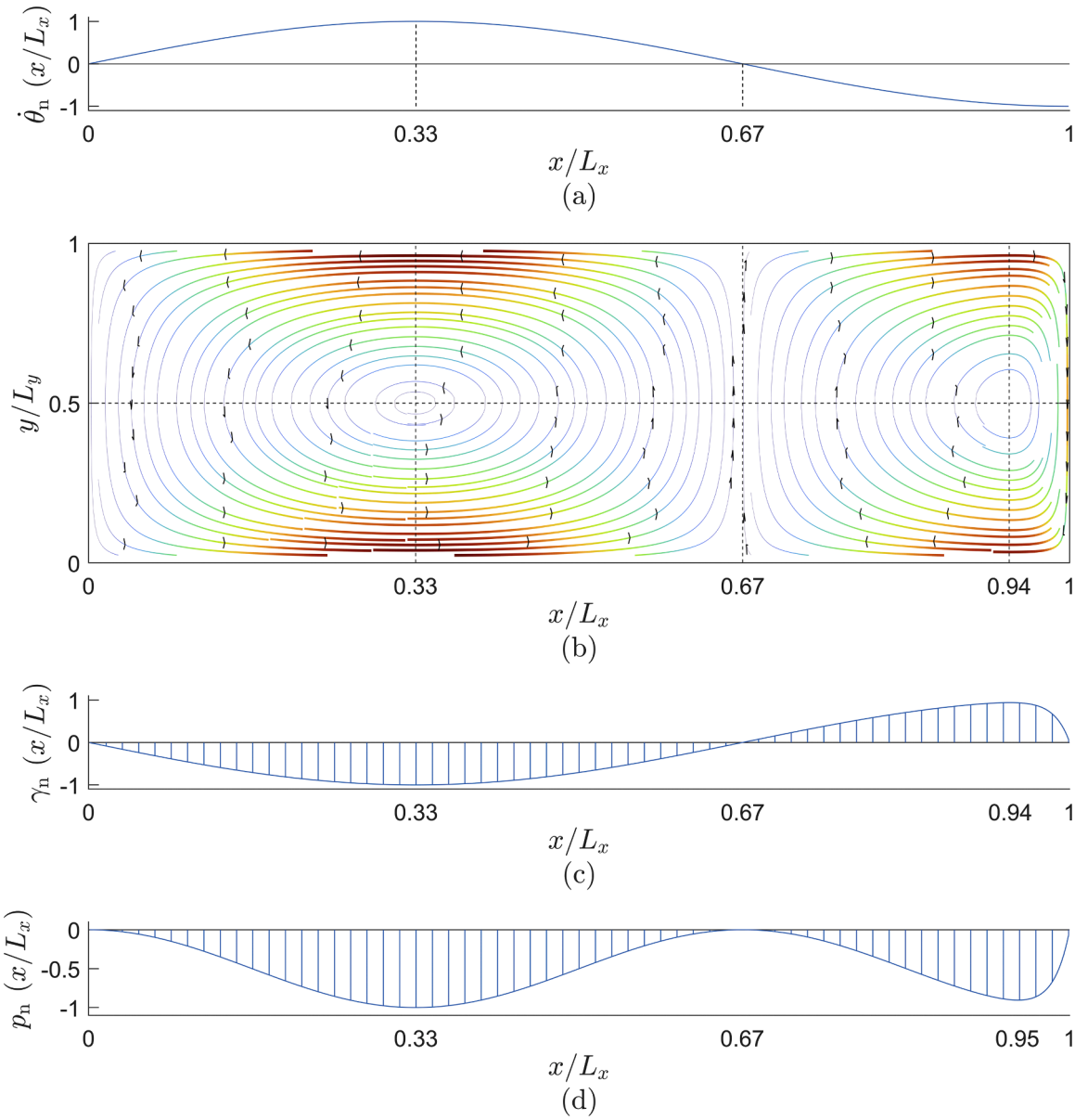

Fig. 16. Parameters for the second mode of Case 5: (a) modal twist velocity; (b) eddy currents density map; (c) normalised torque distribution and (d) normalised power distribution.

- Additionally, the numerical values of the average Joule's losses (P_J) and the average mechanical power (P_m) are equal, as is the case for bending.

4.3.2. Case 5

A static, unitary and uniform magnetic field is applied in the $y-$ direction. Results derived from the normalised modal twist velocity for the first four torsional modes, including eddy currents density map and normalised torque and power distributions, are presented in Figs. 15-18. The maximum values of the normalised variables are indicated in Table 10. Numerical results for the study parameters for each mode are summarised in Table 11.

- Unlike the previous case, only a single row of eddies (**J**) is generated. The number of eddies corresponds to the mode number. Numbering the eddies from left to right, the currents rotate counter-clockwise in odd-numbered eddies and clockwise in even-numbered eddies. The maximum values in the eddy current maps are located at the top and bottom borders of the beam along the $y-$ direction. The eddy centres are positioned at $y = L_y/2$ along the $y-$ direction. In the $x-$ direction, the location of the eddy centres corresponds to the points where the torque distribution reaches a maximum or minimum. For modes 2 to 4, the eddy

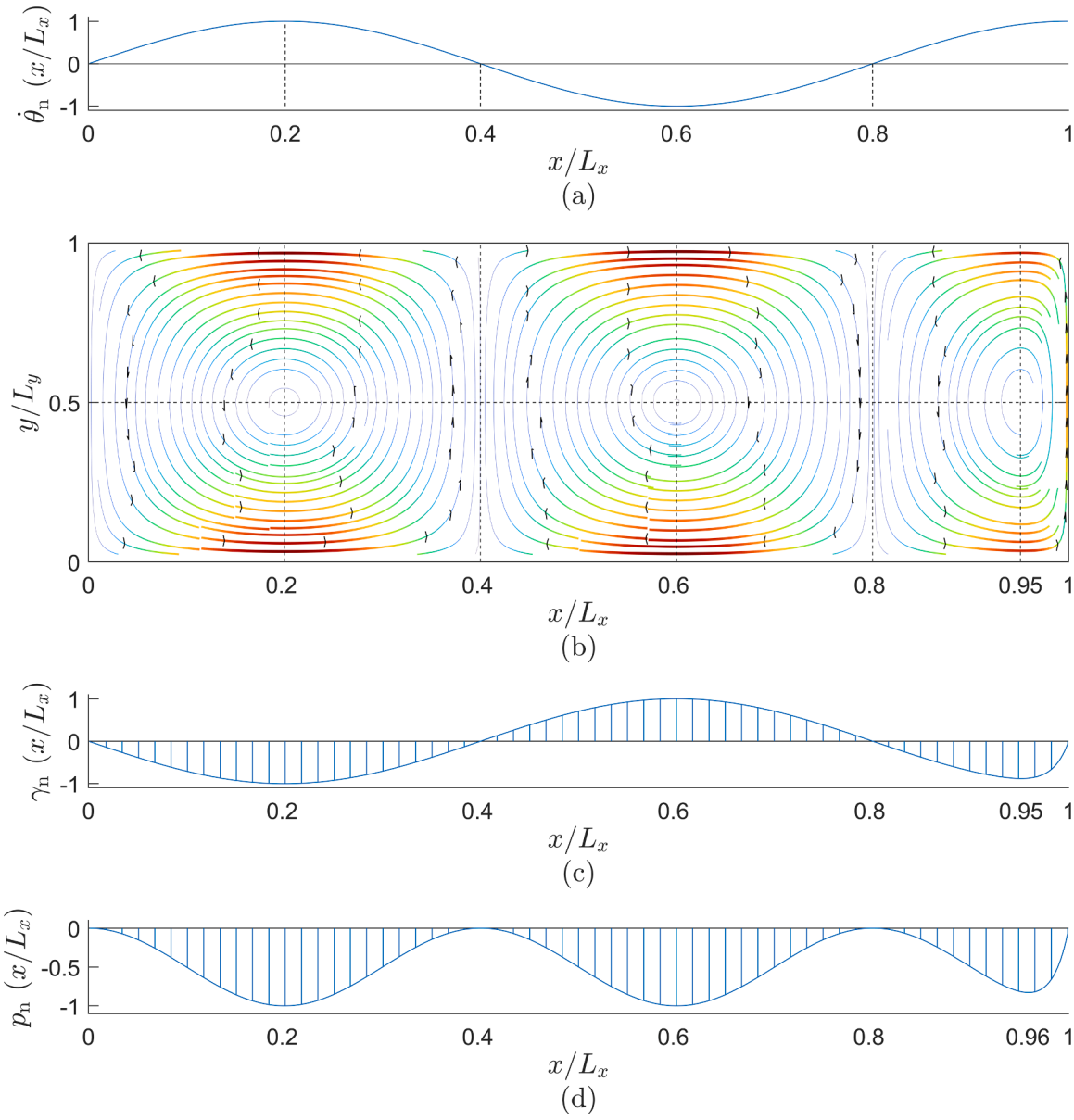

Fig. 17. Parameters for the third mode of Case 5: (a) modal twist velocity; (b) eddy currents density map; (c) normalised torque distribution and (d) normalised power distribution.

borders coincide with the points where the modal velocity is 0, in contrast to previous cases where the border of an eddy coincided with a maximum or minimum in the modal velocity. Although the current density curl at the border of an eddy remains 0, careful examination of Eq. (42) and the applied velocity field given from Eq. (43) reveals that this is only possible when the velocity is zero. As the mode number increases, the eddy centres nearest the fixed end move closer to these ends.

- The torque distribution (γ_{n}) is 0 at both the fixed and free ends of the beam. It is also 0 where the modal velocity is 0 or in the border of an eddy since, at these points, $J_x \approx 0$, and thus, as no external magnetic field acts in the $x-$ direction, the sum in Eq. (31) is 0. Unlike the previous cases, the torque always has the opposite sign of the modal velocity, making it negative near the fixed end, with sign changes occurring at each passage through 0. The locations at which the maximum or minimum values are reached correspond to the eddy centres along the $x-$ direction. This is because the torque in Eq. (31) is only generated by the interaction between J_x and B_y, as indicated in Eq. (29), and at these points J_x is at its maximum or minimum. The maximum torque values presented in Table 10 show an increase from mode 1 to mode 2, followed by a decrease for the higher modes.
- The power distribution (p_{n}) is negative everywhere except at points where it is 0. It is never positive for any mode because the modal twist velocity and torque distribution always have opposite signs, which differs from the previous cases. Similar to the torque distribution, the points where the power distribution is 0 are located at the fixed end, free end, and at the points where the modal

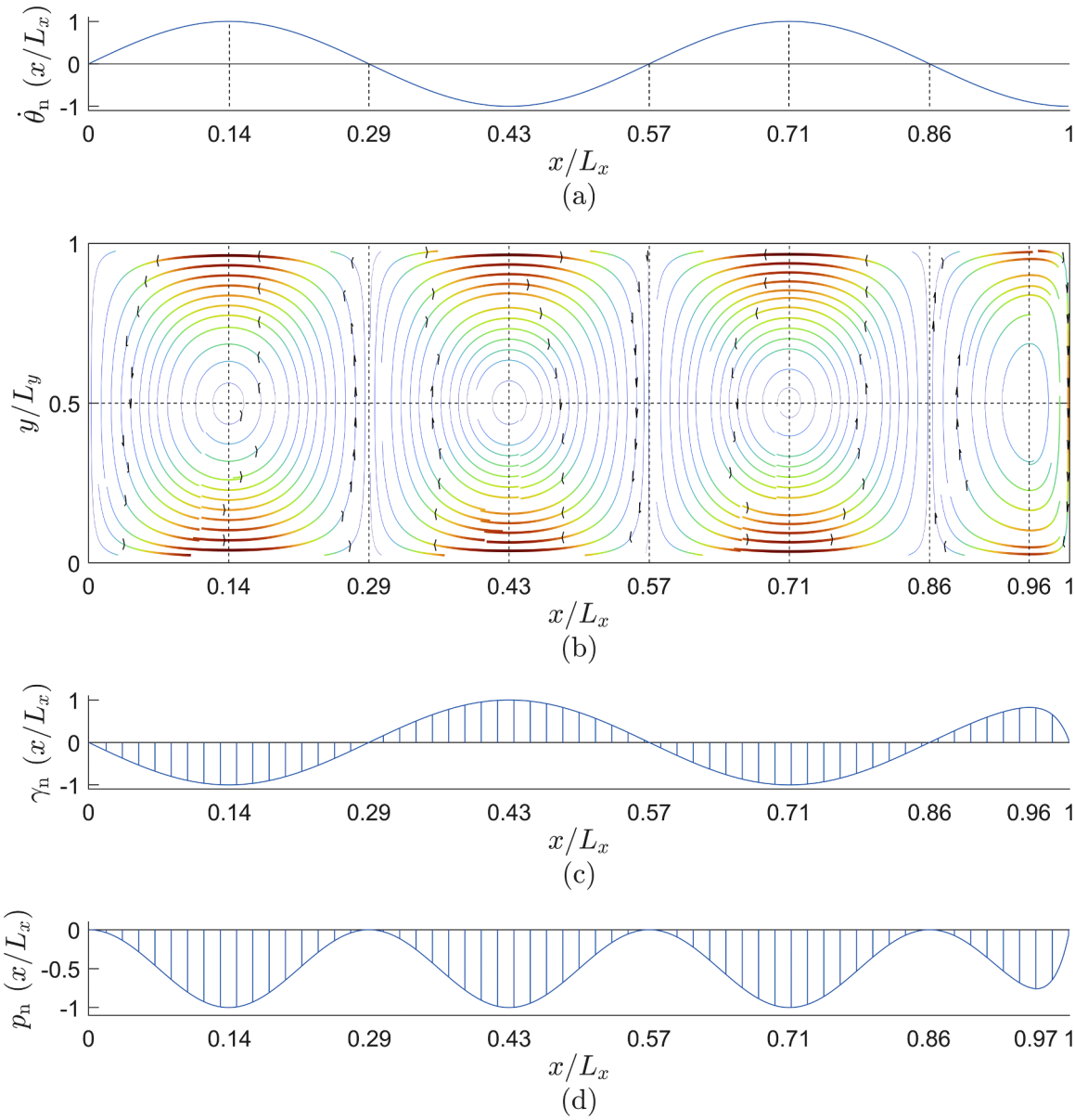

Fig. 18. Parameters for the fourth mode of Case 5: (a) modal twist velocity; (b) eddy currents density map; (c) normalised torque distribution and (d) normalised power distribution.

Table 10
Maximum values of torque and power distributions for each mode of Case 5.

Mode	γ_{max} (Nmmm^{-1})	p_{max} (Wm^{-1})
T1	82.0	8.13
T2	82.7	8.27
T3	81.9	8.19
T4	80.7	8.07

velocity is 0 or at the border of an eddy. At these points $J_x \approx 0$, and as no external magnetic field acts in the $x-$ direction, the sum in Eq. (40) is 0. The minimum values of the power distribution are found at the eddy centres along the $x-$direction which coincide with the locations where the torque distribution is at a maximum or minimum. However, an exception occurs at the eddy centre nearest the free end, where it does not exactly coincide with the minimum value of the power distribution. Since this eddy centre is

Table 11
Resonance frequency, maximum value of the amplitude of the current density map in x and y directions, average power of Joule's losses, average mechanical power, and modal viscous damping ratio for each mode of Case 5.

Mode	ω_r (rads^{-1})	$J_{x_{\max}}$ (MAm^{-2})	$J_{y_{\max}}$ (MAm^{-2})	P_{J} (W)	P_{m} (W)	ζ_r
T1	4578.8	4.70	3.47	−0.805	−0.805	0.193
T2	13736	4.74	3.45	−0.801	−0.801	0.0641
T3	22894	4.70	3.41	−0.793	−0.793	0.0381
T4	32052	4.64	3.35	−0.782	−0.782	0.0268

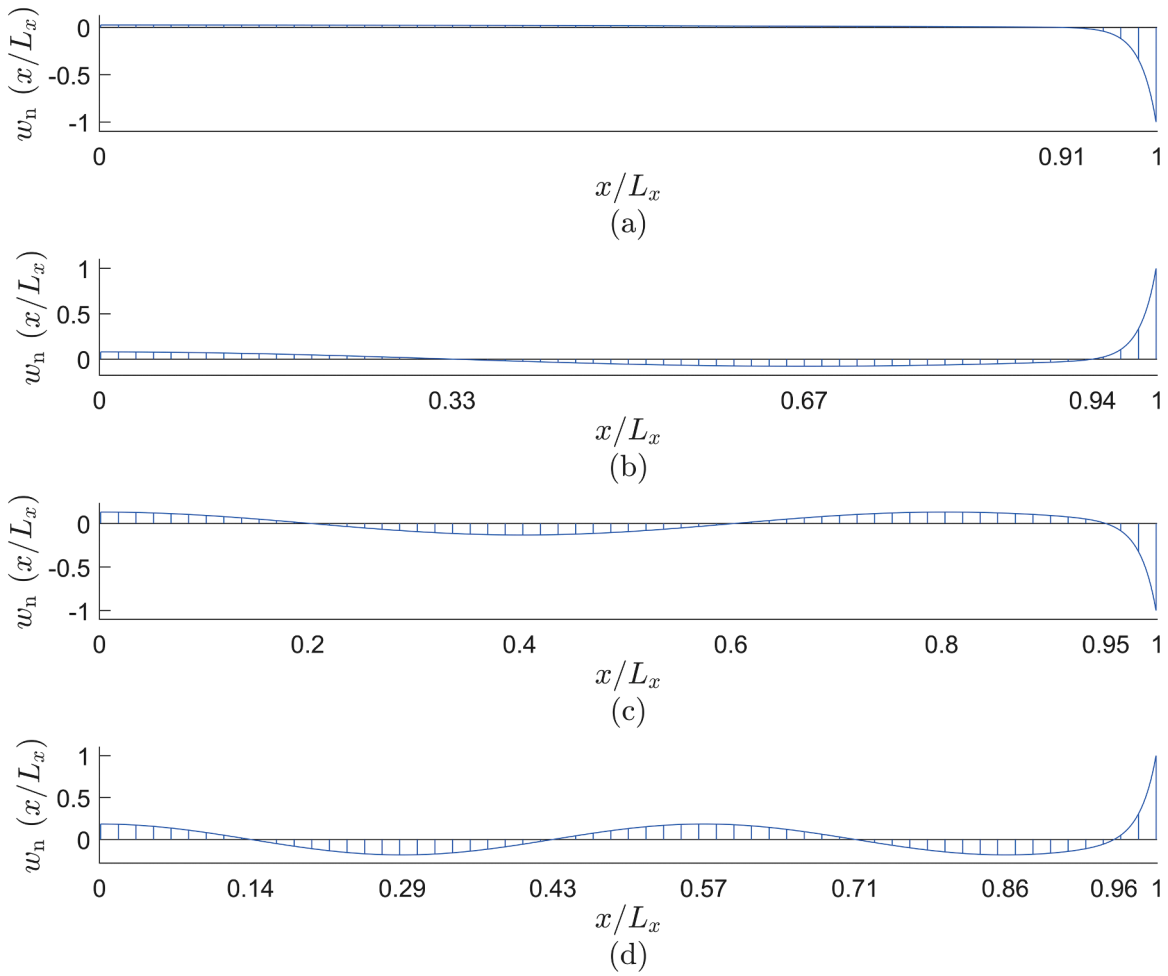

Fig. 19. Normalised transverse force distribution of Case 6: (a) mode 1; (b) mode 2; (c) mode 3 and (d) mode 4.

very close to the free end, this discrepancy is attributed to numerical effects caused by the proximity of the border. According to the values presented in Table 10, the maximum value of the power distribution increases from mode 1 to mode 2, but then decreases.

- All numerical values shown in Table 11 decrease as the mode increases, except for the maximum value of the current density in the $x-$direction ($J_{x_{\max}}$), which increases from mode 1 to mode 2 before decreasing. For torsional motion, when the external magnetic field is applied along the width of the beam, the energy dissipation capability is better at lower frequencies than at higher frequencies because the modal viscous damping ratio (ζ_r) is higher in the lower-order modes. This contrasts with Case 4, where the external magnetic field was applied along the length of the beam.
- The numerical values of the average Joule's losses (P_{J}) and average mechanical power (P_{m}) are equal, as observed in previous cases.

4.3.3. Case 6

The static and uniform external magnetic fields from Case 4 and Case 5 are applied simultaneously. As in Case 3, the application of magnetic fields acting in both the $x-$ and $y-$directions in torsional motion also induces coupling between torsion and bending, as a

Table 12
Maximum values of force distribution for each mode of Case 6.

Mode	w_{max} (Nm^{-1})
T1	24.8
T2	24.7
T3	24.4
T4	24.1

distributed force arises due to the interaction between the magnetic fields and the currents, as described by Eq. (30). In Case 4, the interaction between J_y and B_x does not result in a force distribution, as can be deduced from Eq. (29) and (30), and the same applies to the interaction between J_x and B_y in Case 5. To illustrate the transverse force generated in this scenario, the normalised distribution for the first four modes is shown in Fig. 19, with the maximum values provided in Table 12.

This transverse force arises because, when the external magnetic field is applied in both the $x-$ and $y-$directions simultaneously, the currents lose their symmetry. Similar to Case 3, the analysis of the coupling between the different motions falls outside the scope of this work, and this scenario is not explored further.

5. Conclusions

In this paper, an in-depth study is conducted on the energy dissipation capabilities of eddy currentsgenerated in a thin cantilever beam vibrating within a static and uniform magnetic field under steady-state conditions. A numerical procedure, based on an established finite difference method, has been adapted and utilised to incorporate motional induction.

The beam's motion is described by velocity fields associated with bending or torsional mode shapes. Given that the velocity field is harmonic, the resulting eddy currents are also harmonic. Once these eddy currents are determined, the force distribution, moment distribution, power distribution, Joule's losses, mechanical power, and modal viscous damping ratio are calculated and analysed for a specific beam subjected to an external static and uniform magnetic field applied in various directions.

The results indicate that the direction of the applied magnetic field is a critical factor in vibration applications. The nature of the eddy currents and their dissipative properties vary depending on both the direction of the applied magnetic field and the type of movement. Additionally, it has been demonstrated that the external magnetic field can induce coupling between bending and torsional motions. The findings suggest that, in general, energy dissipation capability is greater for lower-order modes, which is advantageous for mechanical applications aimed at vibration reduction, as certain traditional damping methods often struggle to dissipate energy effectively at lower frequencies.

Declaration of generative AI and AI-assisted technologies in the writing process

During the preparation of this work the authors used ChatGPT in order to improve the language and readability of their paper. After using this tool, the authors reviewed and edited the content as needed and take full responsibility for the content of the publication.

CRediT authorship contribution statement

Mikel Brun: Writing – original draft, Software, Methodology, Formal analysis, Conceptualization. **Fernando Cortés:** Writing – review & editing, Supervision, Methodology, Formal analysis, Conceptualization. **María Jesús Elejabarrieta:** Writing – review & editing, Supervision, Methodology, Formal analysis, Conceptualization.

Declaration of competing interest

The authors declare that they have no known competing financial interests or personal relationships that could have appeared to influence the work reported in this paper.

Acknowledgements

This study has received financial support from the Department of Education of the Basque Government with the Research Group program IT1507-22.

Supplementary materials

Supplementary material associated with this article can be found, in the online version, at doi:10.1016/j.jsv.2024.118787.

Data availability

Data will be made available on request.

References

[1] D.J. Griffiths, Introduction to Electrodynamics, 4th ed., Pearson, Boston, 2013.
[2] A. Gastli, I.A. Metwally, Computation of eddy-current density on ESP motor and well casings under different operating conditions, Simul. Model. Pract. Theory 16 (2008) 483–493, https://doi.org/10.1016/j.simpat.2008.02.002.
[3] M. Amjadian, A.K. Agrawal, A passive electromagnetic eddy current friction damper (PEMECFD): theoretical and analytical modeling, Struct. Control Health Monit. 24 (2017) e1978, https://doi.org/10.1002/stc.1978.
[4] L. Ye, C. Liang, Y. Liu, D. Li, Z. Liu, Performance analysis and test of a novel eddy-current braking & heating system for electric bus, Energy Convers. Manag. 183 (2019) 440–449, https://doi.org/10.1016/j.enconman.2019.01.010.
[5] J. Ruan, L. Dong, J. Zheng, T. Zhang, M. Huang, Z. Xu, Key factors of eddy current separation for recovering aluminum from crushed e-waste, Waste Manag. 60 (2017) 84–90, https://doi.org/10.1016/j.wasman.2016.08.018.
[6] Z. Huang, J. Zhu, X. Wu, R. Qiu, Z. Xu, J. Ruan, Eddy current separation can be used in separation of non-ferrous particles from crushed waste printed circuit boards, J. Clean. Prod. 312 (2021) 127755, https://doi.org/10.1016/j.jclepro.2021.127755.
[7] L. Liang, Z. Feng, Z. Chen, Seismic control of SDOF systems with nonlinear eddy current dampers, Appl. Sci. 9 (2019) 3427, https://doi.org/10.3390/app9163427.
[8] B.B. Shobhana, V.R. Panchal, V.A. Matsagar, Research developments of eddy current dampers for seismic vibration control of structures, J. Vib. Eng. Technol. 12 (2024) 5953–5971, https://doi.org/10.1007/s42417-023-01229-4.
[9] F. Chen, H. Zhao, Design of eddy current dampers for vibration suppression in robotic milling, Adv. Mech. Eng. 10 (2018), https://doi.org/10.1177/1687814018814075.
[10] L. Irazu, M.J. Elejabarrieta, A novel hybrid sandwich structure: viscoelastic and eddy current damping, Mater. Des. 140 (2018) 460–472, https://doi.org/10.1016/j.matdes.2017.11.070.
[11] G.J. Stein, P. Tobolka, R. Chmúrny, Ferromagnetic eddy current damper of beam transversal vibrations, J. Vib. Control 24 (2018) 892–903, https://doi.org/10.1177/1077546316654791.
[12] J.-S. Bae, M.K. Kwak, D.J. Inman, Vibration suppression of a cantilever beam using eddy current damper, J. Sound Vib. 284 (2005) 805–824, https://doi.org/10.1016/j.jsv.2004.07.031.
[13] L.R. Turner, T.Q. Hua, Results for the cantilever beam moving in crossed magnetic fields, COMPEL - Int. J. Comput. Math. Electr. Electron. Eng. 9 (1990) 205–216, https://doi.org/10.1108/eb010076.
[14] D. Rodger, J. Eastham, A formulation for low frequency eddy current solutions, IEEE Trans. Magn. 19 (1983) 2443–2446, https://doi.org/10.1109/TMAG.1983.1062884.
[15] A. Bermúdez, R. Rodríguez, P. Salgado, A finite element method with lagrange multipliers for low-frequency harmonic maxwell equations, SIAM J. Numer. Anal. 40 (2002) 1823–1849, https://doi.org/10.1137/S0036142901390780.
[16] A.Alonso Rodríguez, E. Bertolazzi, R. Ghiloni, A. Valli, Finite element simulation of eddy current problems using magnetic scalar potentials, J. Comput. Phys. 294 (2015) 503–523, https://doi.org/10.1016/j.jcp.2015.03.060.
[17] M. Passarotto, S. Pitassi, R. Specogna, Foundations of volume integral methods for eddy current problems, Comput. Methods Appl. Mech. Eng. 392 (2022) 114626, https://doi.org/10.1016/j.cma.2022.114626.
[18] J. Nagel, Fast finite-difference calculation of eddy currents in thin metal sheets, Appl. Comput. Electromagn. Soc. J. 33 (2018) 575–584.
[19] J.R. Nagel, Finite-difference simulation of eddy currents in nonmagnetic sheets via electric vector potential, IEEE Trans. Magn. 55 (2019) 1–8, https://doi.org/10.1109/TMAG.2019.2940204.
[20] L. Irazu, M.J. Elejabarrieta, Analysis and numerical modelling of eddy current damper for vibration problems, J. Sound Vib. 426 (2018) 75–89, https://doi.org/10.1016/j.jsv.2018.03.033.
[21] R.D. Blevins, Formulas for Natural Frequency and Mode Shape, Krieger Publishing Company, Malabar, Florida, 1995. Repr., reissue 1995, with minor corr.
[22] B.M. Notaroš, Total electromagnetic induction. Electromagnetics, International edition, Pearson, Upper Saddle River, NJ, 2011, pp. 289–294.
[23] J.R. Nagel, Numerical solutions to Poisson equations using the finite-difference method, IEEE Antennas Propag. Mag. 56 (2014) 209–224, https://doi.org/10.1109/MAP.2014.6931698.
[24] L.D. Landau, E.M. Lifshitz, The current density and the conductivity. Electrodynamics of Continuous Media, 2nd ed., rev.enl, Pergamon, Oxford [Oxfordshire] ; New York, 1984, pp. 86–90.
[25] F. Cortés, O. Zarraga, I. Sarría, M.J. Elejabarrieta, Eddy currents damping understood as Zener viscoelastic damping, J. Sound Vib. 547 (2023) 117539, https://doi.org/10.1016/j.jsv.2022.117539.